Tomographic image reconstruction from optical projections in light-diffusing media

S. B. Colak, D. G. Papaioannou, G. W. 't Hooft, M. B. van der Mark, H. Schomberg, J. C. J. Paasschens, J. B. M. Melissen, and N. A. A. J. van Asten

The recent developments in light generation and detection techniques have opened new possibilities for optical medical imaging, tomography, and diagnosis at tissue penetration depths of ~10 cm. However, because light scattering and diffusion in biological tissue are rather strong, the reconstruction of object images from optical projections needs special attention. We describe a simple reconstruction method for diffuse optical imaging, based on a modified backprojection approach for medical tomography. Specifically, we have modified the standard backprojection method commonly used in x-ray tomographic imaging to include the effects of both the diffusion and the scattering of light and the associated nonlinearities in projection image formation. These modifications are based primarily on the deconvolution of the broadened image by a spatially variant point-spread function that is dependent on the scattering of light in tissue. The spatial dependence of the deconvolution and nonlinearity corrections for the curved propagating ray paths in heterogeneous tissue are handled semiempirically by coordinate transformations. We have applied this method to both theoretical and experimental projections taken by parallel- and fan-beam tomography geometries. The experimental objects were biomedical phantoms with multiple objects, including *in vitro* animal tissue. The overall results presented demonstrate that image-resolution improvements by nearly an order of magnitude can be obtained. We believe that the tomographic method presented here can provide a basis for rapid, real-time medical monitoring by the use of optical projections. It is expected that such optical tomography techniques can be combined with the optical tissue diagnosis methods based on spectroscopic molecular signatures to result in a versatile optical diagnosis and imaging technology.

1. Introduction

Recently there has been increased attention on the use of near-infrared (NIR) laser light for imaging the interior of biological tissues.[1] NIR light passes through biological tissue, such as the skull, brain, and breast, and it is well tolerated in large doses because it is nonionizing. In addition, light can be effective in quantifying chemical and molecular states and concentrations, leading to easier identifications of diseased tissue. The noninvasive detection and classification of breast tissues and tumors, based both on the absorbance and the scattering properties of light[1,2] and also on the fluorescence[3] have been described recently. The imaging of the human brain, for monitoring brain oxygenation and detection of brain hemorrhage, has also been investigated.[4] Furthermore, light can also be tagged by ultrasound, another versatile mode of imaging, to make its detection easier.[5]

Optical radiation has actually been used to image tumors by the shadowing effect since the early 1900's.[6] In this technique, called diaphanoscopy,[7] the light is guided by a fiber bundle to an illuminator and the image is recorded by a camera. In breast diaphanography, the difference in the absorption of various tissues enables the detection of the lesions that look darker (dense tumor or hematoma) or clearer (cysts) in the surrounding tissues. A more advanced version of diaphanoscopy has been studied recently with scanned (fiber) laser light.[8] Time-resolved transillumination with short laser pulses has also been studied for the extraction of different tissue parameters for the same application.[9,10] More recently, optical measurements have been extended with light that is modulated at near-gigahertz frequencies, with the expected advantages of better contrast and resolution in the images.[11,12] However,

H. Schomberg is with Philips Research Laboratories, Hamburg, Germany. The other authors are with Philips Research Laboratories, Eindhoven, The Netherlands.

Received 23 April 1996; revised manuscript received 9 September 1996.

0003-6935/97/010180-34$10.00/0

in general, none of the techniques described above provide a reliable distinction factor between healthy and cancerous tissue yet. Considering the widely recognized ease and safety of optical diagnosis methods, further research and development are certainly warranted to bring these optical diagnosis and imaging techniques into a clinically usable stage.

The basic interaction mechanism of optical light with biological tissue is much different from the mechanism by which x rays interact with such tissue. X rays interact with tissue more at the atomic core levels and image primarily the atomic weight differences between different regions. Optical photons, on the other hand, interact and image the electronic level, molecular bonding, and microstructural differences by means of absorption, refraction, or scattering. This can lead to the differentiation of phenomena such as vascularization in a cancer core as well as the molecular differences in the same region, which in turn lead to the detection and assessment of cancer in a noninvasive way that could also be applied to rapid *in vivo* examinations.

Because the generation and distribution of light are much easier than x rays, the data acquisition for optical three-dimensional (3D) tomography can be achieved with much simpler systems than the x-ray computed tomography (CT) systems of today. By using fibers, one can simply guide light to any position or angle on the tissue and collect it from any desired location to analyze spectroscopically by well-established practical methods. Tomographic image reconstruction from light projections, however, is a difficult task because of the strong scattering and diffusion of light in the biological tissue.[13] This diffusion and scattering problem is rather similar to the problem that is encountered in ultrasound diffraction tomography[14] and electrical impedance tomography[15–18] (EIT). One can, in principle, apply some of the techniques that have been used in these tomographic methods[19] to optical tomography. Some of these methods, which are based on algebraic reconstruction techniques (ART's), have actually been employed for the imaging problem in optically diffusive media.[20–24] These approaches, however, require many time-consuming steps and are unstable against noise in the data. Therefore it is not practical to use them in real-time displays of tomographic medical images in the clinical environment.

Our aim in this paper is to describe a tomographic image-reconstruction technique that can be used for 3D mammography in real-time clinical imaging with continuous-wave (cw) light. Our technique described here is based on a modified version of x-ray backprojection tomography. These modifications are applied semiempirically and compensate for the effects of both the diffusion and the scattering of light and the associated nonlinearities in projection-image formation. These methods are based primarily on the deconvolution of the broadened image by a spatially variant point-spread function (PSF) that is dependent on the scattering of light in tissue. The spatial dependence of the deconvolution and nonlinearity corrections for the curved propagating ray paths in heterogeneous tissue are handled by coordinate transformations. We have applied this method to experimental projections taken by parallel-beam and fan-beam tomography geometries on biomedical phantoms with multiple objects, including *in vitro* animal tissue. The results that are presented in this paper demonstrate image-resolution improvements by nearly an order of magnitude. Furthermore, because of the simplicity of our approach, the computation times needed for obtaining useful images are much shorter than those presented previously for this type of problem.[20–24] We also present a basis for more general methods that can lead to improvements in tomographic images if desired at later times.

As a final note in this section, we emphasize that the tomographic method presented in this paper is not a rigorous mathematical inversion technique. Rather, it is an approximate and semiempirical image-restoration technique based on the physics of photon propagation in turbid media and on the well-established signal- and image-processing methods. Numerous examples of these types of approaches can be found in the open literature on general image-reconstruction and image-restoration problems. Some specific examples are deblurring by deconvolution and coordinate transformations in electrical impedance imaging,[18] spatially variant PSF corrections in finite-beam x-ray tomography,[25] beam-width deconvolution in ultrasound imaging,[26] compensation of distance-dependent detector response and photon attenuation in single-photon-emission tomography,[27] restoration of aberrations in astronomical optical imaging systems,[28] and recently even deblurring optical projection images of objects in random multiple-scattering media.[29]

2. Optical Projections in Light-Scattering Media

The main problem with optical imaging techniques in biological tissue is the high amount of light scattering in such media, which tends to blur the projections of light through the tissue because of the associated diffusion of photons. This is demonstrated clearly in Fig. 1, in which the image was obtained by the projection of cw light through an intralipid-solution-filled cell containing the letters PMS (for Philips Medical Systems). In this experiment, a slide of the acronym PMS is immersed in the center of a 10-mm-thick solution of 10% intralipid[30] ($\mu_s' = 1/\text{mm}$). The letter height is 6 mm. NIR laser pulses of 160 fs at the 780-nm wavelength, with ~3-nJ energy per pulse, are used for imaging. The projection in Fig. 1 is obtained when all the photons transmitted through the cell are integrated in time, giving an image that would approximate cw light projection. The transmitted pulse has a total width of ~1 ns. Note the blurring of edge features that is due to the diffusion of photons caused by the scattering from intralipid molecules.

The cw light-projection image shown in Fig. 1 improves considerably if one uses the fastest components of the transmitted pulsed light and generates

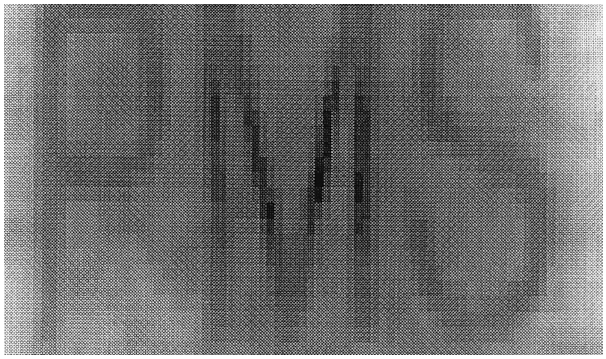

Fig. 1. Image of the acronym PMS (for Philips Medical Systems) immersed in the center of a 10-mm-thick solution of 10% intralipid[30] ($\mu_s' = 1/\text{mm}$). The letter height is 6 mm. NIR laser pulses at the 780-nm wavelength are used for imaging. Here all the photons transmitted through the cell are integrated in time, giving an image that would approximate cw light projection. The transmitted pulse had a total width of ~1 ns.

an image from only these earliest-arriving, ballistic photons.[9] Figure 2 shows the resultant projection image.[30] In this figure, only the first-arriving ballistic photons within the first 12 ps of the transmitted pulse were used to form the image. Note the improvement in image sharpness in Fig. 2 compared with that of Fig. 1. The reason for this is that the earliest-arriving photons have the least amount of scattering in the intralipid solution and therefore result in images with less blurring because of the decreased effects of photon diffusion. However, this pulsed, ballistic imaging method comes at the expense of tedious and costly methods used for this type of imaging. Despite this, such techniques are in experimental trial for the imaging of the internal structure of human tissue[31] and animal organs that cannot be distinguished under cw light projection.

It is important to realize that the improvement in the image shown in Fig. 2 compared with that of the image in Fig. 1 is obtained only owing to the fact that an unscattered component, a ballistic component in the transmitted light within the gated time, is still present. This component is observable because it is larger than the diffusive light at that time period. Increasing the slab thickness will exponentially decrease that component. So after ~15 mm, there is not much improvement in time-gating techniques.

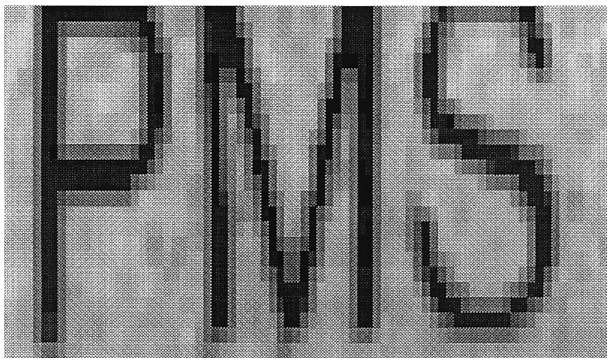

Fig. 2. Image of the same phantom as in Fig. 1, with the acronym PMS, imaged only by the first-arriving ballistic photons. Photons within the first 12 ps of the transmitted pulse were used to form the image. Note the improvement in image sharpness compared with that of Fig. 1 with cw (integrated) light.

Comparable improvements in the sensitivity and sharpness of optical projections can also be obtained when measurements are made with photon density waves that are light modulated at near-gigahertz frequencies.[32] These improvements are primarily due to the attenuation of these waves in diffuse media, which is stronger than the attenuation coefficient of the cw wave at the same fundamental optical wavelength.[33] Obviously similar enhancements in sharpness can also be achieved with an optical wavelength located at a stronger attenuation region for the diffuse media. Both of these latter methods, however, come at the expense of a low transmitted signal-to-noise ratio because of the high attenuation coefficient.[33]

All the experimental techniques for improving the projection image described above come at the expense of low transmitted signals. Therefore, after a limit, the sharpness of the images is compromised by the noise in the image. In principle, however, the quality of the projection image, obtained by the use of any form of light, can also be improved by signal-processing techniques if one quantifies the blurring introduced by the diffusion of light.[13] It is possible to define an approximate PSF for this type of imaging system and to use it to deconvolve and sharpen the raw projection image. Although this would be only a first-order correction, it could provide the basis for a fast optical imaging algorithm suitable for the real-time display of images in a clinical environment. Such a deblurring approach can also provide an initial guess required for more detailed image-reconstruction methods, such as the ART's. In this paper we show that similar image improvements, which have been demonstrated with pulsed or modulated light, can also be achieved in a much easier and improved fashion by the use of image-processing techniques to deblur the cw image to compensate for the diffusion of light.

A. Optical Diffusion in Light-Scattering Media

In this subsection we review and extend some of the main physical principles that apply to photon propagation in diffuse media. As stated above, this is done to quantify the blurring process in order to obtain at least a statistically meaningful PSF that can be used to improve image resolution in diffuse optical tomography.

Suppose that a fiber provides a light input of $I_{\text{in}} = I_o$ (in units of photons per second) into a diffusive medium. Let us assume that this is acting like a point source, radiating photons uniformly in all directions. Then the source term S [in units of photons per (seconds times cubic meters)] is given by

$$S = S_o\delta(\mathbf{r} - \mathbf{r}_S) = I_o\delta(\mathbf{r} - \mathbf{r}_S). \quad (1)$$

In a light-scattering medium such as the intralipid solution discussed at the beginning of this section, the distribution of photons introduced by this source term is governed by the time-dependent transport–diffusion equation[24]:

$$\Delta\varphi(\mathbf{r}, t) - \frac{c\mu_a}{D'}\varphi(\mathbf{r}, t) - \frac{1}{D'}\frac{\partial}{\partial t}\varphi(\mathbf{r}, t) = \frac{-1}{D'}S(\mathbf{r}, t), \quad (2)$$

where $\varphi(\mathbf{r}, t)$ is the photon density distribution (in units of inverse cubic meters), c is the speed of light (in units of meters per second) in the medium, $D' = cD = c/[3(\mu_s + \mu_a)]$ is the photon diffusion coefficient (in units of square meters per second). μ_s and μ_a are the reduced scattering coefficient and the absorption coefficient, respectively (both in units of inverse meters). $S(\mathbf{r}, t)$ is the photon source term (in units of inverse cubic meters times seconds) that injects photons into the medium. This equation has been found to describe well the distribution of photons in highly scattering media with a few heterogeneities.[34] However, it should be noted that its application to problems with real biological tissue is still to be proved.

If one desires to have a solution to the diffusion equation for general object shapes and strengths, there are rigorous analytical and numerical techniques. For example, purely cylindrical or spherical geometries and objects can be handled by analytical techniques. The solution for more complicated geometries, including boundaries, can also be achieved by more general techniques. Many of the numerical examples given in this paper have been done with the public-domain software package[35] PMI (photon migration imaging), which uses such techniques. In addition to semianalytical techniques, one can also solve the diffusion equation by using numerical techniques, such as the finite-element method or the Monte Carlo method. Both of these approaches, however, are computation intensive and time consuming. Keeping in mind that the diffusion equation itself is approximate, one may be able to apply simpler iterative techniques, such as the integral equation approach.[36–38]

1. Homogeneous Media

The solution of the diffusion equation in a homogeneous medium with a time-invariant source S_o (in units of inverse seconds), located at $\mathbf{r}_S$, gives the photon density at a general position $\mathbf{r}$, with[39]

$$\varphi_0(\mathbf{r}) = \frac{S_o}{4\pi D'}\frac{\exp(-\kappa|\mathbf{r} - \mathbf{r}_S|)}{|\mathbf{r} - \mathbf{r}_S|}, \quad (3)$$

where $\kappa = (\mu_a c/D')^{1/2} \sim (3\mu_a\mu_{s'})^{1/2}$. The resulting photon fluence rate $\psi(\mathbf{r})$ (in units of inverse square centimeters times seconds) from this photon density is

$$\psi_0(\mathbf{r}) = \frac{S_o}{4\pi D}\frac{\exp(-\kappa|\mathbf{r} - \mathbf{r}_S|)}{|\mathbf{r} - \mathbf{r}_S|}. \quad (4)$$

Now if we assume that we have a collection area A_0 (in units of square centimeters) at the output fiber and we ignore any corrections that are due to the detector solid angle, then the output intensity I_{out} (in units of photons per second) is

$$I_{\text{out}}(\mathbf{r}) = A_0\psi_0(\mathbf{r}) = \frac{S_o A_0}{4\pi D}\frac{\exp(-\kappa|\mathbf{r} - \mathbf{r}_S|)}{|\mathbf{r} - \mathbf{r}_S|} \quad (5)$$

To be able to probe a medium, the measurements are made at a specific set of detector positions $\mathbf{r}_D$ to obtain the output intensity as a result of propagation of light from another set of source positions $\mathbf{r}_S$.

The output intensity equation, Eq. (5), however, does not provide a direct assignment of the value of this intensity back to the object real space in this media. For that, we look at photon path distributions, which are given by the response of the system for a point perturbation in the medium. This is studied in Subsection 2.A.2 for a point object.

2. Point Object

Point Absorber: Let us first assume that we have an absorbing point object at position $\mathbf{r}_1$ within the scattering medium. The total photon density at position $\mathbf{r}$ in the medium changes because of the presence of this point perturbation to a value given by[39,40]

$$\varphi(\mathbf{r}) = \varphi_0(\mathbf{r}) + (-q)\alpha_1(\mathbf{r}, \mathbf{r}_1), \quad (6)$$

where $-q$ is a parameter that indicates the strength (in units of meters) of the point absorber according to its radius and absorption coefficient, and the perturbation part of the photon density $\alpha_1(\mathbf{r}, \mathbf{r}_1)$ (in units of inverse meters to the fourth) is given by

$$\alpha_1(\mathbf{r}, \mathbf{r}_1) = \frac{S_o}{4\pi D}\frac{\exp(-\kappa|\mathbf{r}_1 - \mathbf{r}_S|)}{|\mathbf{r}_1 - \mathbf{r}_S|}\frac{\exp(-\kappa|\mathbf{r}_1 - \mathbf{r}|)}{|\mathbf{r}_1 - \mathbf{r}|}. \quad (7)$$

Using the previous set of expressions and rearranging, we find

$$\varphi(\mathbf{r}) = \varphi_0(\mathbf{r})\left[1 - q\frac{\alpha_1(\mathbf{r}, \mathbf{r}_1)}{\varphi_0(\mathbf{r})}\right] = \varphi_0(\mathbf{r})[1 - qP(\mathbf{r}, \mathbf{r}_1)], \quad (8)$$

where the simplified expression for the perturbation part $P(\mathbf{r}, \mathbf{r}_1)$ is given (in units of inverse meters) by

$$P(\mathbf{r}, \mathbf{r}_1) = \frac{\exp[-\kappa(|\mathbf{r}_1 - \mathbf{r}_S| + |\mathbf{r}_1 - \mathbf{r}| - |\mathbf{r} - \mathbf{r}_S|)]}{|\mathbf{r}_1 - \mathbf{r}_S|\,|\mathbf{r}_1 - \mathbf{r}|/|\mathbf{r} - \mathbf{r}_S|} \quad (9)$$

Contour and surface plots of the functional form of this perturbation function are given in Fig. 3 for source and detector positions at $\mathbf{r}_S = (-a, 0, 0)$ and $\mathbf{r}_D = (a, 0, 0)$, where the parameters $a = 50$ mm and $\kappa = 0.175$/mm are used as examples. These plots are given only for the $z = 0$ plane, and the actual 3D shape of the perturbation function $P(\mathbf{r}, \mathbf{r}_1)$ can be obtained by the rotation of the shape in the $z = 0$ plane around the x axis.

The plots in Fig. 3 basically represent the effect of a point absorber, of strength $q(\mathbf{r}_1)$ located at $\mathbf{r}_1/a$ in the object space (note that $\mathbf{r}_1$ now scans the whole of the object space), on the propagation of light from a

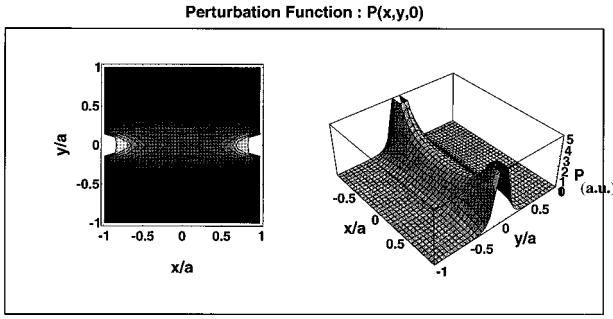

Fig. 3. Spatial dependence of the perturbation function $P(\mathbf{r})$ on a small point absorber is shown in the $(x/a, y/a, 0)$ plane for $\mathbf{r}_S = (-a, 0, 0)$, $\mathbf{r}_D = (a, 0, 0)$.

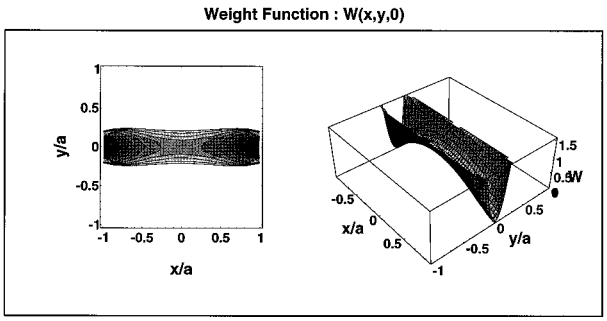

Fig. 4. Spatial dependence of the weight function $W(\mathbf{r})$, which represents the inverse assignment of a perturbation strength that causes an observed measured transmitted intensity difference at a detector position $\mathbf{r}_D$. The plot is in the $(x/a, y/a, 0)$ plane. The source and detector locations are $\mathbf{r}_S = (-a, 0, 0)$ and $\mathbf{r}_D = (a, 0, 0)$, respectively.

source located at $\mathbf{r}_S = (-a, 0, 0)$ to a detector located at $\mathbf{r}_D = (a, 0, 0)$.

Note that the meaning of the perturbation function $P(\mathbf{r}, \mathbf{r}_1)$ is that if an intensity (or photon density) measurement differs from an expected value, then the cause of this difference can be assigned to any point in the object space according to this function. In fact, the strength of the perturbation $q(\mathbf{r}_1)$ that causes the observed difference is inversely proportional to the value of $P(\mathbf{r}, \mathbf{r}_1)$.

Let us now assume that we have made a measurement at a detector position $\mathbf{r}_D$, giving a value for the perturbation as $P(\mathbf{r}_D, \mathbf{r}_1)$. We now assign perturbation strength values to the whole object space, giving a possible $q(\mathbf{r}_1)$ distribution for all possible $\mathbf{r}_1$ within this space. For notational simplicity, letting $q(\mathbf{r}_1) \rightarrow q(\mathbf{r})$ (that is, $\mathbf{r}_1 \rightarrow \mathbf{r}$) in the equations above, we get

$$q(\mathbf{r}) = \frac{1}{P(\mathbf{r}_D, \mathbf{r})}\left[1 - \frac{\varphi(\mathbf{r}_D)}{\varphi_0(\mathbf{r}_D)}\right] \tag{10}$$

or

$$q(\mathbf{r}) = \frac{1}{P(\mathbf{r}_D, \mathbf{r})}\,\frac{\varphi_0(\mathbf{r}_D) - \varphi(\mathbf{r}_D)}{\varphi_0(\mathbf{r}_D)} = W(\mathbf{r}_D, \mathbf{r})\,\frac{\Delta\varphi(\mathbf{r}_D)}{\varphi_0(\mathbf{r}_D)}, \tag{11}$$

where the difference in the measured and the expected values of the transmitted intensity is

$$\Delta\varphi(\mathbf{r}_D) = \varphi_0(\mathbf{r}_D) - \varphi(\mathbf{r}_D), \tag{12}$$

and the weight function (in units of meters) is

$$W(\mathbf{r}_D, \mathbf{r}) = \frac{1}{P(\mathbf{r}_D, \mathbf{r})} = \frac{|\mathbf{r}_1 - \mathbf{r}_S|\,|\mathbf{r}_1 - \mathbf{r}_D|/|\mathbf{r}_D - \mathbf{r}_S|}{\exp[-\kappa(|\mathbf{r}_1 - \mathbf{r}_S| + |\mathbf{r}_1 - \mathbf{r}_D| - |\mathbf{r}_D - \mathbf{r}_S|)]}. \tag{13}$$

The plot of this weight function, which is given in Fig. 4, represents the spatial dependence of the strength of the perturbation $q(\mathbf{r})$ at each position $\mathbf{r}$ in object space, which could account for the measured intensity difference $\Delta\varphi(\mathbf{r}_D)$ at the detector position $\mathbf{r}_D$. The parameters used in this figure are identical to those of Fig. 3. The spatial variations in the form of the weight function, as seen in Fig. 4, can be divided into two parts: The first part is the longitudinal component [described by the numerator in Eq. (13)] along the line from the source to the detector, and the second part is the transverse part [the denominator in Eq. (13)] that identifies the curvature of this function perpendicular to the line from the source to the detector. In the studies that are described in this paper, we have assumed that the variations in the longitudinal component are much smaller than the variations in the transverse direction. This is a good assumption for positions away from the sources and detectors. Therefore, in most of our studies, the longitudinal variations have been ignored because the objects of interest to us were sufficiently removed from the edges of the image space. As seen in Fig. 4, the weight function variations along the source–detector line are strong only near the edges of the image space close to the source–detector points. The transverse part describes the main contribution to the blurring function in the shape of a banana extending from the source to the detector and this is described in Subsection 2.A.3.

Point Scatterer and Absorber: Using a perturbation theory,[36–38] we can extend the result given above to the case in which the point absorber is replaced by a point object that is different from the background medium in both its absorption and scattering coefficients. The result for the photon density perturbation can be given by the following simplified expression for the far-field effects:

$$\alpha_1(\mathbf{r}_S, \mathbf{r}_D, \mathbf{r}) = \frac{-S_o}{4\pi D}\left[\mathbf{p}(\mathbf{r} - \mathbf{r}_S)\cdot\frac{(\mathbf{r}_D - \mathbf{r})}{|\mathbf{r}_D - \mathbf{r}|} + q\right] \times \frac{\exp(-\kappa|\mathbf{r} - \mathbf{r}_S|)}{|\mathbf{r} - \mathbf{r}_S|}\,\frac{\exp(-\kappa|\mathbf{r} - \mathbf{r}_D|)}{|\mathbf{r} - \mathbf{r}_D|}, \tag{14}$$

where $q(\mathbf{r})$ is the chargelike term and $\mathbf{p}(\mathbf{r} - \mathbf{r}_S)$ is the dipolelike term, with a direction defined by the location of the scatterer with respect to the source. This term is calculated when the shape of the scatterer

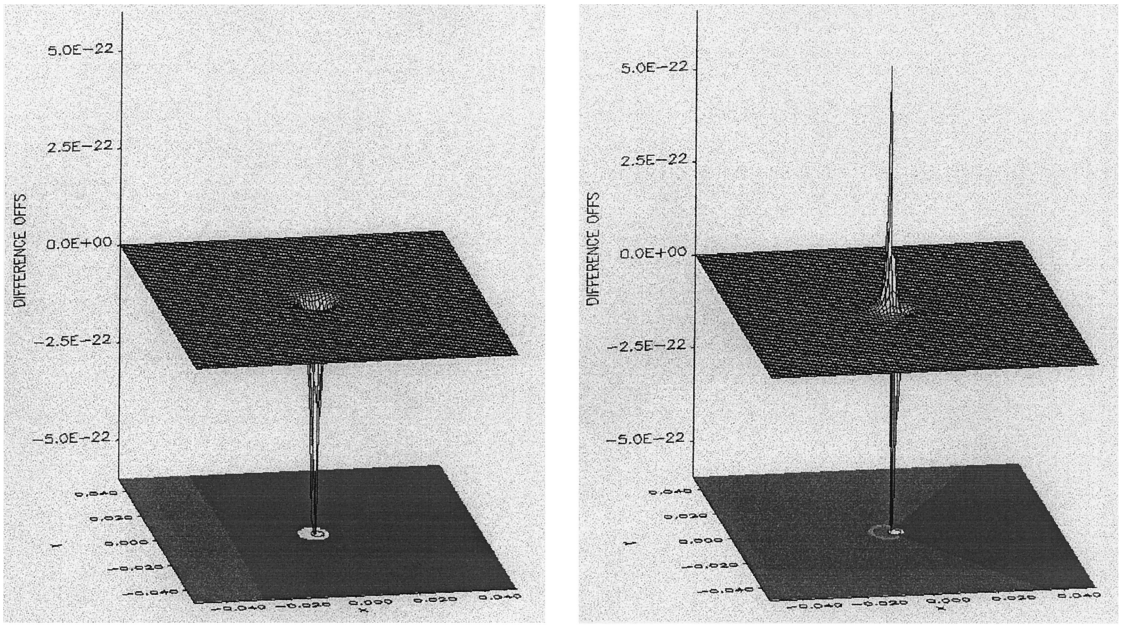

Fig. 5. Perturbed part of the photon density computed within the diffusion theory for (a) a small absorber, (b) a small scatterer, with a source located at position 0.0 on the y axis for each case. The results are plotted only to demonstrate the chargelike and dipolelike effects of these perturbations of absorbing and scattering objects. The quantitative parameters are not relevant for the present discussion.

and the gradient of the photon density that is the photon current are taken into account.[36–38] For a small spherical, isotropic scatterer, the direction of the dipole is given simply by $(\mathbf{r} - \mathbf{r}_S)/|(\mathbf{r} - \mathbf{r}_S)|$, as discussed in Ref. 38. A pair of opposite point charges, aligned according to the shape and the relative position of the scatter with respect to the source, approximate a dipole. Therefore, with this approximation, in reconstruction problems q could be represented, for example, by the nodal values of the charges and $\mathbf{p}$ could be represented by the mesh values of the dipolar charges. The direction of the mesh, then, affects the perturbation field, as can be calculated from the simplified expression given above. The charge and the dipole nature of small absorbing and scattering inhomogeneities, respectively, are illustrated in Fig. 5.

The main implication of the expression given above is that, other than the directional dependence in the dipole term, the main shape of the distribution of the perturbation photon density field is still given by the perturbation function shape discussed in Subsection 2.A.1. This means that the examples we give below for absorbing bodies could also be extended to the more general case of the scattering and the absorbing inhomogeneities. Especially for the parallel-beam projection geometry discussed in Subsection 2.B, such extensions are straightforward. In this geometry, both the source-to-perturbation $(\mathbf{r} - \mathbf{r}_S)$ and the perturbation-to-detector $(\mathbf{r} - \mathbf{r}_D)$ vectors are nearly collinear. Therefore the shape of the blurring function is nearly identical for any type of perturbative object. For an arbitrary set of vector directions, such as that encountered in the fan-beam geometry, the dipolar nature of the scattering is evident in the projections, although its effects tend to cancel mainly in the process of tomographic summation. Despite this, more information about the objects can be obtained if the dipolar nature of the scattering is handled separately in the projections. Such an analysis leads to two sorts of images, one for the scattering inhomogeneities and the other for absorbing inhomogeneities. These issues will be discussed further in another paper.

3. *Banana-Shaped Light Paths*

Regardless of which technique is used, it is found that the highest probability paths of photons between a source and a detector in diffuse media is confined to banana-shaped regions.[40] In a highly heterogeneous medium, such regions can have complicated shapes. However, for the example we have studied above for a point absorber, such a banana region is defined by[40]

$$B(\mathbf{r}) = P(\mathbf{r}_D, \mathbf{r})/P(a, 0, 0; x, 0, 0), \tag{15}$$

where $P(\mathbf{r}_D, \mathbf{r})$ is the perturbation function discussed above for the given example for source and detector locations of $\mathbf{r}_S = (-a, 0, 0)$ and $\mathbf{r}_D = (a, 0, 0)$; $P(a, 0, 0; x, 0, 0)$ is its value along the line that connects the source and the detector, that is, for our example, along the x-axis,

$$B(\mathbf{r}) = \frac{\dfrac{\exp[-\kappa|\mathbf{r} - (-a)\hat{x}|]}{|\mathbf{r} - (-a)\hat{x}|}\dfrac{\exp(-\kappa|\mathbf{r} - (a)\hat{x}|)}{|\mathbf{r} - (a)\hat{x}|}}{\dfrac{\exp[-\kappa|x - (-a)|]}{|x - (-a)|}\dfrac{\exp[-\kappa|x - (a)|]}{|x - (a)|}}.$$

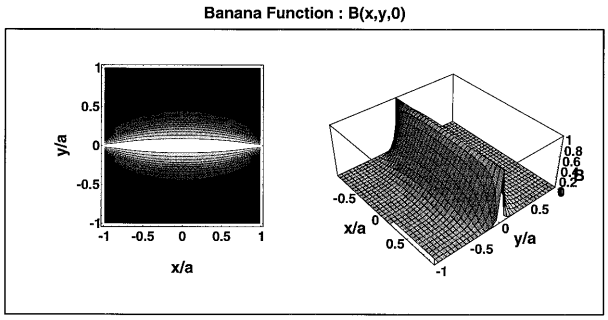

Fig. 6. Spatial dependence of the banana function $B(\mathbf{r})$ that represents the amount of blurring introduced in images in diffuse media. The plot is in the $(x/a, y/a, 0)$ plane. The source and the detector locations are $\mathbf{r}_S = (-a, 0, 0)$ and $\mathbf{r}_D = (a, 0, 0)$, respectively.

A two-dimensional (2D) plot of this equation is shown in Fig. 6. The corresponding 3D shapes are obtained simply by the rotation of these images around the symmetry axis of the banana. It is clear that the resolution of imaging in diffusive media depends on the width of these banana-shaped regions, regardless of how distorted they may be.

The banana function varies rapidly close to sources and detectors, but it has a relatively constant width in the middle, away from the source and the detector positions. Therefore it causes a spatially dependent broadening of the projection images through diffuse media. This position dependence is shown in Fig. 7 for different locations along the line from the source to the detector.

As implied in Fig. 6, the projections of the objects embedded in diffusive media will be blurred. It is also clear that this blurring will be a function of the distance from the source–detector points. Furthermore, the blurring will depend on the strength and the shape of the object(s) because the imaging process itself is a nonlinear process. The shape of the banana function depends on the medium itself and therefore on the distribution of objects.[41] Overall,

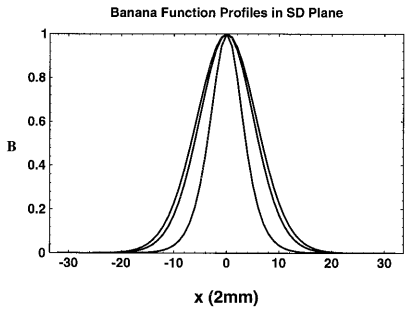

Fig. 7. Density profile of $B(\mathbf{r})$ as a function of transverse dimension x of the contour picture shown in Fig. 6 for different distances from the source. These profiles are given approximately at distances of $3(\mathbf{r}_S - \mathbf{r}_D)/6$ (center of banana), $2(\mathbf{r}_S - \mathbf{r}_D)/6$, and $(\mathbf{r}_S - \mathbf{r}_D)/6$ (closest to the source–detector) for the outermost, middle, and inner curves, respectively, where $(\mathbf{r}_S - \mathbf{r}_D) = 100$ mm. Note that the width of the banana does not change rapidly unless the area of interest is very close to a source or a detector.

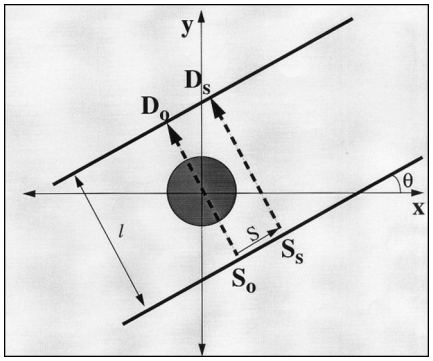

Fig. 8. Parallel-beam projection geometry for obtaining the optical image of an object. The plane in the figure shows the (x, y) plane of a Cartesian coordinate system. The object is an infinite cylinder centered at the origin, $\mathbf{r} = \{0, 0, 0\}$, and its cross section is indicated as the darker circle in the middle. The object is characterized with optical parameters μ_s', μ_a, and n. This object is embedded in an infinite medium with optical parameters μ_{s0}', μ_{a0}, and n_0.

this will result in a complex convolution matrix[42] that blurs the images obtained by the transmittance of light through the medium. Nevertheless, one can improve the resolution of images by using a set of spatially dependent approximated deconvolution in the image space and by performing empirical corrections for the imaging nonlinearities. In fact, as we show below, such an empirical approach is a much more practical and faster way for improved tomography in diffusive media compared with ART-based methods.

B. Parallel-Beam Projections

In this subsection we define the main parameters and the geometry used in taking projection images through an optical medium. If the medium is transparent with only absorption inhomogeneities, then the projections are identical to those taken by x rays. The projections through scattering media are highly broadened as we discussed already in Subsection 2.A.

The geometry for the parallel-beam projections is given in Fig. 8. To illustrate our tomography approach, we consider a case in which an optically diffusive infinite cylinder with radius $r = 5$ mm is placed at the origin. In this example, because the object is cylindrically symmetric, its projections at different angles θ will be the same. We consider general object shapes below in this paper, after the basics of our approach are described.

Note that we can define a projection space (s, θ) as indicated with the parameters in Fig. 8. The angle θ is defined as the angle of the source or the detector lines with respect to the xy axes. The parameter s is the shortest distance of the source–detector line to the origin of the (x, y) space. Then the transformation between the coordinates of these two spaces, that is, the object space (x, y) and the projection space (s, θ), is defined with

$$s = x \cos \theta + y \sin \theta. \tag{16}$$

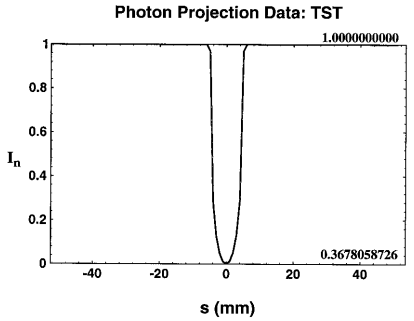

Fig. 9. Example of intensity projection in transparent media, TST. This projection data is for a theoretical phantom with a more absorbing cylindrical object of 5-mm radius embedded in a homogeneous nonabsorbing medium. The numbers on the right axis give the maximum and the minimum quantitative values for this graph.

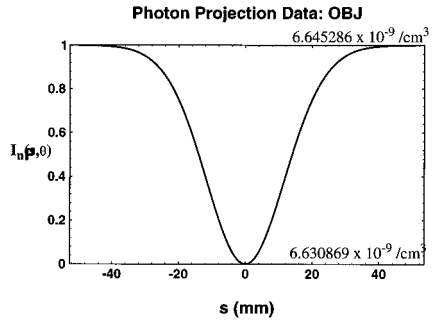

Fig. 10. Light-projection data for a theoretical phantom with a scattering cylindrical object, OBJ, embedded in a scattering medium. The optical parameters of this system are given in Table 1. Parallel-beam projection geometry is used for obtaining the optical image of an object. The object is an infinite cylinder centered at the origin $\mathbf{r} = \{0, 0, 0\}$. The numbers on the right axis give the maximum and the minimum quantitative photon density values for this graph.

Note that once the projection angle θ and the (x, y) location in the object space are given, then the coordinates in the (s, θ) space are defined by Eq. (16).

1. *Transparent Media: X-Ray Projections*

If a medium is transparent, that is, it has only absorption inhomogeneities and no scattering, then the projections through such a medium are similar to those that can be taken by x rays. In this case the transmitted intensity through the medium is given by

$$I(s, \theta) = I_0 \cdot \exp\left[\int_L \mu_a(x, y, E, t)\mathrm{d}l\right], \qquad (17)$$

where I_0 is the input source intensity and μ_a is the attenuation coefficient, which has spatial dependence and can also depend on the energy of the photons E and can be time dependent. Assuming that we have a steady-state and energy-independent attenuation, Eq. (17) transforms to the transmittance or the projection expression given by

$$I_n(s, \theta) = \frac{I(s, \theta)}{I_0} = \exp\left\{-\int_{-s}^{s}\int_{-s}^{s}[\mu_a(x, y) \times \delta(x\cos\theta + y\sin\theta - s)]\mathrm{d}x\mathrm{d}y\right\}. \qquad (18)$$

We give the shape of the projection for a 5-mm-radius inhomogeneity in a transparent medium in Fig. 9. We use this example to be able to compare such x-ray projections with the corresponding ones that are given below for diffuse media. For our simple projection example, taken in the projection geometry of Fig. 8, the attenuation constant is assumed to be zero except inside a cylinder with a 5-mm radius. Therefore all projections are identical to the one for $\theta = 0°$. Because this is used only for demonstration purposes, the exact value of this attenuation coefficient is not important.

In matrix notation, the transformation from the object space to the projection space given by the expression in Eq. (18) can be represented in a general form as $\mathbf{I} = \mathbf{hM}$, where $\mathbf{I}$ and $\mathbf{M}$ represent the projected intensities and the medium absorption coefficients, respectively, and $\mathbf{h}$ is the matrix that represents the Radon transform between these quantities. In the diffuse optical projections, this transformation matrix $\mathbf{h}$ is dependent on the medium itself, resulting in a nonlinear system of equations. This form of representation is used in Subsection 3.A to develop a unified framework for reconstructive imaging methods in order to put our approach in this paper in the right perspective within the tomography field.

2. *Projections in Diffuse Media*

The projection examples given for the diffuse media uses the same parallel-beam projection geometry given in Fig. 8. For the first example, we assume that all the optical coefficients of the cylinder are identical to the surrounding diffusive media except that its absorption coefficient μ_a is 1% higher. Otherwise these optical coefficients are $\mu_s' = 1.0/\mathrm{mm}$, $\mu_a = 0.01/\mathrm{mm}$, and $n = 1.5$. Taking the distance between the source–detector separation as $l = 100$ mm, we obtain the projection of photon density transmission at the detector side by using the PMI software package[35] for the solution of the diffusion equation in Eq. (2). The results are shown in Fig. 10. In this example, because the object is cylindrically symmetric, its projections at different angles θ will be the same. We consider general object shapes below in this paper, after the basics of our approach are described.

The projection profile of the absorbing cylindrical object in Fig. 10 is compared with another projection profile obtained with a much thinner cylindrical object in Fig. 11. This latter projection represents the PSF of the diffuse medium in this example. Note that the projection profiles are almost identical, implying that the actual shape of the object itself is

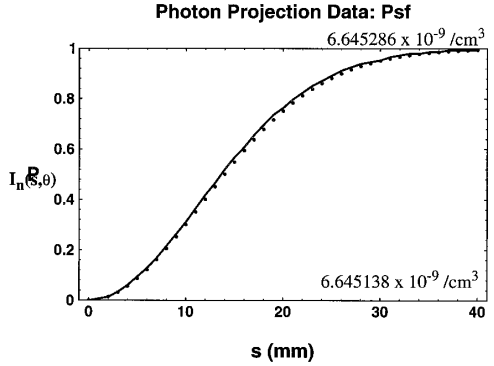

Fig. 11. Comparison of the light-projection data with a large cylinder from Fig. 10 (dotted curve) with those of a much smaller cylinder (solid curve) that represent the PSF of the background scattering medium. The optical parameters are given in Table 1. The numbers on the right axis give the maximum and the minimum quantitative values for this graph (which apply only to the solid curve). The dotted curve is redrawn from Fig. 10 for comparison purposes, and therefore the quantitative values do not apply on that projection.

highly blurred with this PSF. The optical parameters used in this example, along with those for the transparent media in Subsection 2.B.1 and those in diffuse media with a stronger inhomogeneity are given in Table 1.

Now let us take a closer look at the intensities observed in taking a projection. For this we consider again the simple case of an absorbing point perturbation that results in a photon density expression, as given in Eq. (6). Replacing $\mathbf{r}$ with $\mathbf{r}_D$ for the detector and $\mathbf{r}_1$ with $\mathbf{r}$ for a general position for the perturbation and integrating over the object space for all possible positions of the perturbations that could affect the observed intensity at the detector position, we get

$$I_{\text{out}}(\mathbf{r}_D) = \frac{I_{\text{in}}}{4\pi D_0}\frac{\exp(-\kappa_0|\mathbf{r}_D - \mathbf{r}_S|)}{|\mathbf{r}_D - \mathbf{r}_S|} \times \left\{1 - \frac{1}{V_n}\int_{\text{Vol}} [q(\mathbf{r})P(\mathbf{r}_D, \mathbf{r})]\mathrm{d}\mathbf{r}\right\} \quad (19)$$

where S_0 is replaced by I_{in} and V_n is the normalization constant (in units of cubic meters) for the distribution of the perturbation function. Noting that, for the parallel-beam projection geometry, all source–detector distances are equal, that is, $\mathbf{r}_{SD} = |\mathbf{r}_S - \mathbf{r}_D|$ for all source–detector pairs, we get

$$I_{\text{out}}(\mathbf{r}_D) = I_{\text{in}}C_0\left\{1 - \frac{1}{V_n}\int_{\text{Vol}} [q(\mathbf{r})P(\mathbf{r}_D, \mathbf{r})]\mathrm{d}\mathbf{r}\right\}, \quad (20)$$

where C_0 is a constant, independent of spatial position. Comparing this equation with the one obtained for the x-ray projections in Eq. (18), we see that in optical tomography, what we effectively obtain is that the line integral for the x-ray absorption is replaced by the volume integral for the diffuse optical attenuation. This volume is actually defined within the volume of the banana function discussed above.

For optical attenuation in diffuse media as well, we can define a projection space, in a simplified 2D geometry, and obtain the intensities as

$$I_n(s, \theta) = \frac{I_{\text{out}}(s, \theta)}{C_0 I_{\text{in}}} = 1 - \iint \{q(x, y)P_n[\mathbf{r}_D, (x, y)]\}\mathrm{d}x\mathrm{d}y, \quad (21)$$

where we have also normalized the detected intensity to the input intensity. The normalization constant V_n, defined above, has now been absorbed in the definition of the normalized perturbation function $P_n[\mathbf{r}_D, (x, y)]$. We can calculate this for angle = 0°, and all other angle projections are the same as this one because of the cylindrical symmetry.

3. *Spatially Dependent Blurring and Nonlinearities*

As can be seen in the above set of figures, the projections in diffuse media are broadened by an amount determined by the optical constants of the media. It is important to realize the fact that the amount of broadening is also a function of the location of the object and its strength. The diffusion results in nonlinear image formation in the projections. This is illustrated in the projection profiles given in Fig. 12 for four different cases corresponding to two cylinders with different absorption coefficients located at two different positions in the diffuse medium, as illustrated in the intensity projections shown in the figure.

4. *Physical Quantities for Parallel Projection Tomography*

In x-ray tomography, the intensity projections are usually converted into the attenuation coefficient κ values before the operations of tomographic image reconstruction. Normally the quantity plotted in x-ray tomography is the attenuation coefficient distribution. The attenuation value is then found with Eq. (18). The result is

$$\kappa_{\text{xray}}(s, \theta) = \frac{I_P(s, \theta)}{L} = \frac{\ln[I_0/I(s, \theta)]}{L}, \quad (22)$$

Table 1. Optical and Geometrical Parameters of the Object and the Phantom

Parameter	Object—OBJ	Object—PSF	Test—TST[a]
$\mu_{s0} = \mu_s$ (1/mm)	1.0000	1.0000	—
μ_{a0} (1/mm)	0.0100	0.0100	0.0000
$n_0 = n$	1.5	1.5	—
μ_a (1/mm)	0.0101	0.0101	0.100
κ_0 (1/mm)	0.173205	0.173205	0.0
$\Delta\kappa_{\max}$ (1/mm)	0.000864	0.000864	—
$\kappa_0 + \Delta\kappa_{\max}$ (1/mm)	0.174069	0.174069	—
$\mathbf{r}$ (mm)	5.0	0.5	5.0

[a]TST, transparent media.

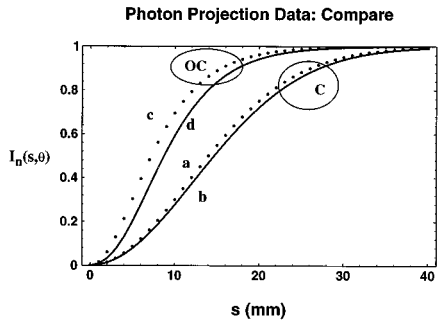

Fig. 12. Light projections that show the effect of object (cylinder) position and the strength of perturbation on the intensity projection shape. These demonstrate the effects of the spatially dependent blurring and the nonlinear image formation. The projections for the same object as shown in Figs. 10 and 11, OBJ, are drawn as dotted curves, the one on the right (circle labeled C) is for a centered object, and the one on the left (circle labeled OC) is for an off-centered object that is closer to a source line than to the detector line. The solid curves represent corresponding projections for another cylinder with the same parameters, except that its absorption coefficient is 50 times higher than that of the previous cylinder. In summary, a is the reference centered cylinder with weak absorption. Solid curve b shows what happens to the shape of the projection if the strength of the absorption is increased by a factor of 50. Dotted curve c and solid curve d show the shape of the projection if the weakly and the strongly absorbing cylinders, respectively, are moved off center to a position 10 mm away from the source line. The strongly absorbing cylinders distort the projection rays around themselves and result in the indicated difference as compared with a weak cylinder. This is a direct demonstration of the nonlinearities in the projection image formation.

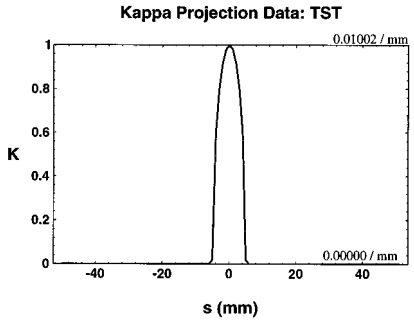

Fig. 13. X-ray normalized attenuation coefficient K projection that corresponds to the intensity projection in Fig. 9. The numbers on the right axis give quantitative values. These values are used in the text to compute contrast in the images.

where, in this case, the absorption μ_a is replaced by the x-ray attenuation coefficient κ_{xray}. CT values are usually displayed in a unit relative to the attenuation of water. The x-ray intensity projection of Fig. 9 is converted into attenuation projection by the use of these relationships, and the resultant attenuation coefficients are normalized by

$$K = \frac{\kappa(s, \theta) - \kappa_{\min}}{\kappa_{\max} - \kappa_{\min}}, \tag{23}$$

where $\kappa_{\max}$ and $\kappa_{\min}$ are the maximum and the minimum values of the attenuation coefficient κ_{xray} data, respectively. The final projections are shown in Fig. 13.

Background Attenuation κ_0 in Diffuse Media: There are many possible quantities that could be used as the imaged quantity in optical tomography in diffuse media. These possibilities are the attenuation coefficient, absorption or scattering coefficients, the diffusion coefficient, the perturbation parameters $q(\mathbf{r})$ or $\mathbf{p}(\mathbf{r})$, the differences of such parameters at two wavelengths, their time dependences and constants, etc. For us, in this paper, the preferred quantity for the final projections is the attenuation coefficient κ. As we see below, such a quantity is needed anyway to quantify the blurring in the images. Absolute values of the background attenuation coefficient κ_0 for diffuse optical tomography can be found first by the assumption of a homogeneous medium. In the present case, in which we have limited our discussion to cw light, we can obtain this value by taking measurements at two or more different source–detector distances near homogeneous regions. With this we have two different source–detector distances, $r_1 = |r_{D1} - r_{S1}|$ and $r_2 = |r_{D2} - r_{S2}|$. We then use Eq. (5), replacing $\mathbf{r}$ with $\mathbf{r}_D$ for these two distances, which results in measured intensities of I_1 and I_2. By taking ratios of these intensities, (I_1/I_2), we get

$$\kappa_0\big|_{21} = \frac{1}{r_2 - r_1} \ln\left(\frac{I_1 r_1}{I_2 r_2}\right) = \frac{\ln(I_2 r_2) - \ln(I_1 r_1)}{r_2 - r_1} \tag{24}$$

for these two sets of source–detector pairs. If there are variations of κ_0 for different measurements from different source–detector pairs, we then can take their maximum (or average) value and proceed for the tomographic operations that need this quantity. Note that Eq. (24) ignores any boundary effects.

Attenuation Fluctuations $\Delta\kappa(s, \theta)$ in Diffuse Media: Depending on whether we take the maximum, average, or minimum attenuation constant as the background, we can then define the variations in the attenuation coefficient $\Delta\kappa(s, \theta)$. For the parallel-beam projection geometry, we can do this by taking measurements at different source–detector pairs with equal distances, but obviously probing different locations in the medium. We then have two different source–detector pairs, $r_{ij} = |r_{Di} - r_{Sj}|$ and $r_{kl} = |r_{Dk} - r_{Sl}|$ with equal total source–detector distances, $r_{SD} = r_{ij} = r_{kl}$, resulting in measured intensities of I_{ij} and I_{kl}. By applying Eq. (5) and assuming that the diffusion constant (scattering coefficient) variations have a much smaller effect on the projection fluctuations than the attenuation constant changes, we get

$$\begin{aligned}\kappa(s, \theta) &= \kappa_{ij-00} \\ &= \kappa_0 + \frac{1}{r_{SD}} \ln\left(\frac{I_{00}}{I_{ij}}\right) \\ &= \kappa_0 + \frac{1}{r_{SD}} \ln\left[\frac{I_{00}}{I(s, \theta)}\right],\end{aligned} \tag{25}$$

where we define the space dependence $\kappa(s, \theta)$ of the attenuation coefficient on the projections by referring

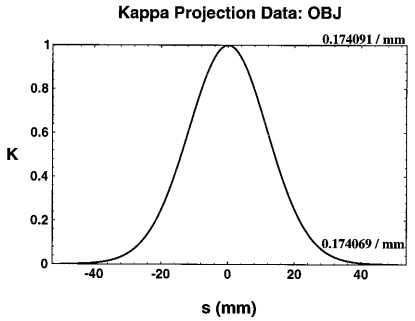

Fig. 14. Normalized attenuation coefficient K projection that corresponds to the diffuse intensity projection in Fig. 10. The numbers on the right axis give quantitative values.

the (ij)th source–detector measurements to the measurement (00)th that represents the background value in the previous subsection.

Our simplification above, on our ignoring the variations in the diffusion constant, warrants an explanation. We note that the main parameter that defines the magnitude of this constant is the scattering coefficient. The relative magnitude of the changes in this scattering coefficient in biological tissue is expected to be small. Furthermore, for equal amounts of a resultant perturbed photon density, a scattering point acts like a dipole source. The combined effect of the two opposite charges making up the dipole, from a scattering coefficient difference, has been found to be weaker than a single equivalent charge term coming from the absorption differences.[40] We are currently studying these assumptions and related ones in taking other projection parameters, and the results of our findings will be reported elsewhere.

The diffuse intensity projection of Fig. 10 is converted to an attenuation constant projection by the use of the approach described above. These absolute values are normalized by Eq. (23). The final projection in terms of these normalized attenuation coefficient values are shown in Fig. 14.

The dependence of the attenuation coefficient on the strength and the location of the perturbation is shown in Fig. 15 for the centered and the off-centered cylinders (see Fig. 12) with weak and strong absorption coefficient differences with respect to the background. This figure indicates the dependence of the diffusion blurring on the spatial location and the strength of the perturbation, indicating the nonlinearities in the image formation. These differences are more easily observable if the same projections are shown in normalized attenuation coefficients, as in Fig. 16.

C. Fan-Beam Projections

The parallel-beam projection geometry, discussed in the previous sections up to now, provides a simpler arrangement for the mathematical procedures of the backprojection tomography. However, for experimental simplicity, one prefers to make measurements in a fan-beam geometry, in which the image

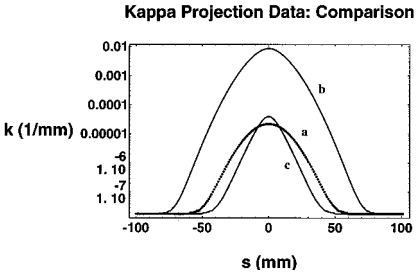

Fig. 15. Absolute values of the attenuation coefficient projections for cylinders of 5-mm radius in the same medium as in the previous figures. The background attenuation coefficient (0.173205/mm) has been subtracted from these projections. These correspond to the intensity projections given in Fig. 12. The labeling is as follows: centered cylinder with weak absorption (curve a, 1% perturbation), centered strong absorption (curve b, $\times 50$ perturbation), and an off-centered weak absorption (curve c, 1% perturbation, $\sim$10 mm away from the source line).

area is enclosed in an array of source–detector pairs located on the periphery of a circular area. In this section we present the properties of the projections in the fan-beam geometry.

The geometry for the fan-beam projections is given in Fig. 17. In our computations and in our experimental system that is described in Section 4, we take 32 source and 32 detector positions equally spaced and interlaced on the periphery of a 10-cm-diameter cylindrical phantom. Each raw projection is defined as the collection of data measured as photons transmitted from a source to all 32 detectors on the periphery of a circle around this cylinder.

It should be realized that the fan-beam projection geometry in Fig. 17 can also be transformed into the parallel-beam projection geometry. The only difference in this transformed (s, θ) space of the fan-beam projections compared with our previous (s, θ) projection space in the parallel-beam geometry is that the s and the θ parameters in the fan-beam geometry are coupled and cannot be varied independently. With the source–detector geometry we have chosen, it

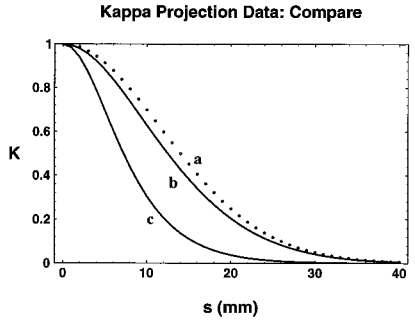

Fig. 16. Normalized values of the attenuation coefficient projections for cylinders of 5-mm radius as in Fig. 15. Dotted curve a is the reference centered cylinder with weak absorption. Solid curve b shows what happens to the shape of the projection if the strength of the absorption is increased by a factor of 50. Solid curve c shows the shape of the projection if the weakly absorbing centered cylinder is moved off center, as in Fig. 12.

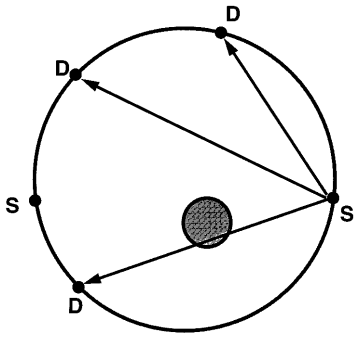

Fig. 17. Fan-beam projection geometry that shows the arrangement of sources and detectors schematically. The source and the detector locations are equally spaced on the periphery of the circular area. In the numerical examples and the experiments that are described below, we take 32 equally spaced source positions and 32 equally spaced detector positions. The source and the detector locations are interlaced with respect to each other.

turns out that the separations between different s coordinates probed at a given θ decrease as one goes away from the $s = 0$ projection. The effect of this is that the edges of the phantom are probed with higher resolution because of this crowding of the projections.

Note that we can also define our projection space within the fan-beam tomography according to the angles of the source and the detector locations with respect to, for example, the x axis. We can then define this as the source–detector index, or (ϕ_S, ϕ_D), projection space. In this case, we can simply take the source index i_S and the detector index j_D and plot our projections as a function of these indices. We number our detector indices j_D as referenced from the source index i_S for a given projection. Note that, for the geometry given in Fig. 17 in which the sources and the detectors are equally spaced on the periphery, these indices directly correspond to equally spaced angles ϕ_{Si} and ϕ_{Dj} for the corresponding positions.

In order to illustrate our tomography approach in the fan-beam geometry, we consider a case in which an optically absorptive infinite cylinder with radius $r = 5$ mm is placed within the object space in a diffuse medium. We consider general object shapes below, after the basics of our approach are described. We assume that all the optical coefficients of the cylinder are identical to the surrounding diffusive media except that its absorption coefficient μ_a is higher. Otherwise these optical coefficients are $\mu_s' = 3.0$/mm, $\mu_a = 0.01$/mm and $n = 1.5$. These parameters are summarized in Table 2. Taking the proper arrangement of the source–detector locations, we obtain the projection of photon density transmission at the detector side by using the PMI software package[35] for the solution of the diffusion equation. The analysis of what we see from the projections is the same as with the parallel-beam projections, that is, the observed intensity $I_{\text{out}}(\phi_S, \phi_D)$ at a detector position is simply given by the expression for $I_{\text{out}}(\mathbf{r}_S, \mathbf{r}_D)$ in Eq. (20).

The results of intensity projections in (ϕ_S, ϕ_D) space normalized to a maximum intensity value of unity (the whitest part the figure) are shown as a 2D gray-level plot in Fig. 18. The top and the bottom light areas correspond to intensities measured with closest source–detector positions. Note that, with this plotting, we cannot notice any inhomogeneities because the intensities decay radially owing to point sources and exponentially to attenuation. Therefore the intensity readings at large source–detector distances are much smaller than the intensity readings at small source–detector distances. In order to get around this problem and observe the effects of inhomogeneities in intensity projections, one can normalize each projection that corresponds to a unique j_D individually and replot the projections after such a normalization. This would bring the inhomogeneities up to an observable level.

Table 2. Optical and Geometrical Parameters of the Object and the Phantom

Parameter	Object—OBJ
$\mu_{s0} = \mu_s$ (1/mm)	3.000
μ_{a0} (1/mm)	0.0100
$n_0 = n$	1.5
μ_a (1/mm)	0.500
κ_0 (1/mm)	0.3
$\Delta\kappa_{\max}$ (1/mm)	2.1
$\kappa_0 + \Delta\kappa_{\max}$ (1/mm)	2.4
$\mathbf{r}$ (mm)	2.5

Find an Effective κ_0 in Diffuse Media: As we discussed above, the preferred quantity for imaging is the attenuation coefficient. The attenuation coefficient κ values for the optical tomography for the fan-beam geometry can be found by the use of the values of the measurements at two or more different source–detector distances. This is easier to apply for the fan-beam geometry because of the large amount of variation in the effective source and detector distances. In fact, as we discussed above, this variation

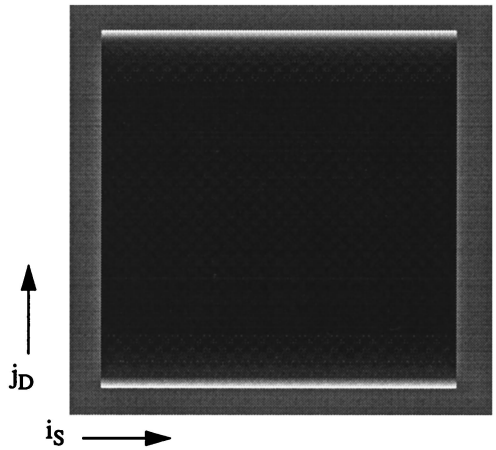

Fig. 18. Fan-beam light-projection data in $(\phi_S, \phi_D) = (i_S, j_D)$ space for a theoretical phantom with a scattering cylindrical object, OBJ, embedded in scattering media. The optical parameters of this system are given in Table 2.

causes a large dynamic range in the measured intensities.

The dependence of the measured intensities on the attenuation, diffusion, and distances in a homogeneous phantom is given by Eq. (5). Using this for two different source–detector distances, $r_0 = |r_{D0} - r_{S0}|$ and $r_1 = |r_{D1} - r_{S1}|$, which result in measured intensities of I_0 and I_1, and by taking ratios of these intensities (I_0/I_1), we get

$$\kappa_0|_{10} = \frac{1}{r_1 - r_0} \ln\left(\frac{I_0 r_0}{I_1 r_1}\right) = \frac{\ln(I_1 r_1) - \ln(I_0 r_0)}{r_1 - r_0}.$$

By finding all κ_0 values corresponding to all possible source–detector combinations, that is, I_1 for $r_1 = |r_{D1} - r_{S1}|$ relatively with respect to I_0, we end up with a range of κ_0 that reflects the inhomogeneities and boundaries in our object region. And if there are variations of κ_0 for different measurements, we can take their maximum or average value and proceed for the tomographic operations that need this quantity, as described in the next subsection. In summary, the procedure described above gives the background attenuation $\kappa_{0,\mathrm{ave}}$ to which the actual measurements are referenced.

Find Fluctuations $\Delta\kappa(s, \theta)$ *in Diffuse Media:* For the tomographic quantity of interest, depending on whether we take the maximum, average, or the minimum, we also have to define the variations in the tomographic quantity, such as the attenuation coefficient, $\Delta\kappa(s, \theta)$, by simply referring the individual values of the attenuation coefficient κ calculated above for various $r_1 = |r_{D1} - r_{S1}|$ that correspond to different source–detector pairs to the value of the background attenuation $\kappa_{0,\mathrm{ave}}$. We perform this as follows: First we compute an effective reference intensity I_{00} that would be measured at a reference distance r_{00}, which we chose to be small (much smaller than any measurement distances) by using the background attenuation coefficient $\kappa_{0,\mathrm{ave}}$ found above. For this we use the average of all I_{00} found from all possible combinations of (i, j) indices. As above, we assume that the diffusion constant (scattering coefficient) variations have a much smaller effect on the projection fluctuations than the attenuation constant changes do. As pointed out above, this assumption is a valid one for turbid media that approximate the biological tissue. Using these reference values, we calculate the effective attenuation coefficient fluctuations from

$$\Delta\kappa_{ij} = \kappa_{ij} - \kappa_{0,\mathrm{ave}} = \frac{\ln(I_1 r_1) - \ln(I_{00} r_{00})}{r_1 - r_{00}} - \kappa_{0,\mathrm{ave}}. \quad (26)$$

The results of the conversion of the projections from intensity values to attenuation coefficient values are shown with the 2D gray-level plot in Fig. 19 in (ϕ_S, ϕ_D) space normalized to a maximum attenuation value of unity (whitest in the figure).

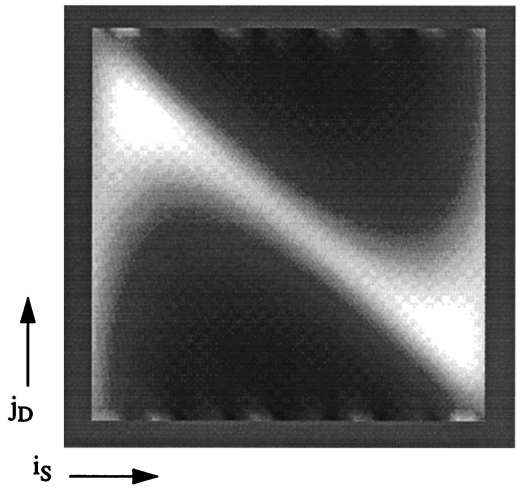

Fig. 19. Normalized fan-beam attenuation projection data K in $(\phi_S, \phi_D) = (i_S, j_D)$ space for a theoretical phantom with a cylindrical object, OBJ, embedded in scattering media. This figure is obtained from the intensity projection data in Fig. 18 by the use of the procedure described in the text for the attenuation constant calculations in fan-beam geometry.

3. Optical Tomography in Diffuse Media: Theoretical

From the examples studied in Section 2, it is clear that a direct use of the optical projections in the reconstruction of images of diffuse media will result in highly broadened and distorted images. In this section, the main topic is the description of semiempirical methods that compensate for these effects in the imaging process. These methods, which are presented in the subsections below, however, are based on simplified, partly heuristic assumptions about the propagation of light in tissue. These assumptions lead to relatively simple reconstruction algorithms based on deconvolution in the Fourier space within the bounds of x-ray backprojection tomography. This semiempirical approach is chosen simply to be able to achieve a fast algorithm for optical image reconstructions that could be applied to real-time imaging of the human body.

Before we discuss the details of our simplified semiempirical tomographic approach, we first outline the basics of the methodology that applies to image reconstruction from projections in a general way. Such a unified framework for reconstructive imaging methods, as outlined in the Subsection 3.A, puts our method in this paper in the right perspective within the tomography field. At the end of Subsection 3.A, we hope to make it clear that the more general and rigorous treatments of the image-reconstruction problem, especially for diffuse media, lead to time-consuming and highly noise-susceptible algorithms without any superior results, at least not yet. Such rigorous treatments of the diffuse tomography problem are still in their research phases and are not yet suitable for practical clinical applications.

A. Unifying Framework for Reconstructive Imaging Methods

The general approach for the solution of image reconstruction from projections is based on the unifying

framework for reconstructive imaging methods promoted in Ref. 19 and proceeds as follows:

First, we identify a suitable physical experiment that is to be used to gather information about the object to be imaged. One needs to know the laws that govern the interaction of the radiation with the object, the exact geometry of sources and detectors, and the exact physical meaning of the quantities being emitted and received. In our case, the radiation is light, the governing laws might be formulated in the form of a diffusion equation with appropriate initial and boundary conditions, and the quantity being emitted and received might be interpreted as a photon flux density wave. We may distinguish between the ac case, in which one uses time-modulated waves, and the stationary dc case, in which one observes stationary flux densities.

Second, we set up an accurate mathematical model of the physical experiment identified in the first step. It should be possible to formulate the model as an integral operator $M: X \rightarrow Y$ from one function space X (containing functions that represent the possible objects) to another function space Y (containing functions that represent the possible observations). The general form of the model is

$$(Mf)(y) = \int_{\mathrm{Vol}} \{K[x, y; f(x)] f(x)\} \mathrm{d}x, \qquad (27)$$

where x is the position vector, Vol is the volume occupied by the object, $f(x)$ is the function that represents the object, y is a generalized coordinate that characterizes the emitted radiation and the source–detector positions, and $K[x, y; f(x)]$ is a kernel that describes how much $f(x)$, the object at position x, contributes to $(Mf)(y)$, the observed value at generalized coordinate y. The experiment provides a sampled and error-contaminated approximation to the function Mf. Computing Mf is referred to as the forward problem. In the ac case, the model may be obtained from the underlying diffusion equation and the associated initial and boundary conditions by means of a Green's function. In the dc case, other considerations[43] lead to a kernel that describes integration over banana-shaped volumes. The form of the model in Eq. (27) is useful for the following steps, but it is not mandatory. In our case, other formulations involving the diffusion equation directly could also be used. Strictly speaking, the model is not unique. For example, one could linearize an otherwise nonlinear model by replacing the kernel in Eq. (27) by a kernel of the form $K[x, y; f_o(x)]$, where $f_o(x)$ represents a standard object, such as a homogeneous background medium. The resulting model is, of course, less accurate.

Third, given the model derived in the step above, we study the determinacy of the inverse problem: How well is the object determined by the model and the observations? The crucial questions to be answered (if possible) are (1) Is the model invertible? That is, do ideal data determine the object uniquely? If not, change experiment and model so as to collect more independent data (if possible). (2) Because of the integrating action in Eq. (27), the model will have a smoothing property. The unpleasant effect of the smoothing property is that it spoils the determinacy of the object: Rather different objects can yet give rise to fairly similar observations. One says that the inverse problem is ill posed. How strong is the smoothing property? If it is strong, then real data, which are inevitably incomplete and error contaminated, cannot well determine the object, even if ideal data would. Often the smoothing property depends on the laws governing the propagation of the radiation, and if so, it may not be possible to change the smoothing property. The answers to these questions are often difficult to find, but in our case, we can borrow results obtained in related disciplines: The ac case has a formal similarity with ultrasonic and electromagnetic imaging methods based on inverse scattering.[14] The linearized version of the inverse scattering problem (Born's approximation) is analytically tractable, allowing one to identify the conditions on the model (and hence the experiment) under which a meaningful reconstruction ought to be possible. The smoothing property depends on the wavelengths employed. In the biomedical applications of our interest, that wavelength is of the order of 5 cm, implying a theoretical resolution of slightly less than 1 cm.[44] The dc case has a formal similarity with EIT. The reconstruction problem of EIT has been studied with some success. It is known that the model is invertible[17] and that it has a strong smoothing property.[43]

Finally, we can devise a reconstruction algorithm that reconstructs the object as well as possible. Many approaches are possible. If the inverse operator M^{-1} exists and is explicitly known, one may apply it to the observed data. In our case, good models are nonlinear, and then there is no chance of knowing the inverse operator in explicit form. In this situation, one is left with solving, in some way or other, the equation $Mf = g$, where g is a function that describes the observed data. At some stage, discretization will be necessary. Eventually one will end up with a discrete system of equations to be solved by some suitable algorithm. If M is linear, the resulting system of equations will be also linear so that it may be written in the form

$$\mathcal{A} \cdot \mathbf{u} = \mathbf{b}, \qquad (28)$$

where $\mathcal{A}$ is a matrix and $\mathbf{u}$ and $\mathbf{b}$ are vectors. Note that this notation is changed with respect to the one we used in defining projections in Subsection 2.B.1. If $\mathbf{h}$ as defined in Subsection 2.B.1 is nonlinear, the form of Eq. (28) will be

$$\mathcal{A}(\mathbf{u}) \cdot \mathbf{u} = \mathbf{b}(\mathbf{u}) \qquad (29)$$

where $\mathbf{u}$ is a vector and $\mathcal{A}(\mathbf{u})$ and $\mathbf{b}(\mathbf{u})$ are matrix- and vector-valued functions of $\mathbf{u}$, respectively. The inevitable smoothing property of the model will also make it necessary to apply some form of regularization.

This term refers to techniques that prevent undue oscillations in the reconstructed function. When the smoothing property is strong, much regularization is required and the achievable resolution is poor. When the model is not invertible, then a reconstruction in the strict sense of the word is not possible. All one can do is to construct an object that could explain the observations, but there is, in general, no guarantee that this object has anything to do with the true object.

There is a plethora of numerical algorithms for solving ill-posed, discrete linear equations of the form of Eq. (28). When $\mathcal{A}$ is a huge matrix (a common situation in image reconstruction), most of the textbook algorithms are ruled out. A notable exception is the Kaczmarz method,[45] an iterative method that acts on the rows of the matrix one at a time (and hence it can handle huge matrices). The Kaczmarz method, which has been reinvented several times and is also known as the ART, may be generalized for solving nonlinear equations of the form of Eq. (29). Another candidate is a class of methods known as projections onto convex sets.[46] When the system to be solved is less huge (or the available computer is fairly big), many other methods become feasible, such as the conjugate gradient method or the Newton–Raphson method. These methods can also be adapted to a formulation of the reconstruction problem without an integral operator of the form of Eq. (27). In any case, regularization has to be built in, in some way or other. Incidentally, all the methods mentioned above have already been applied in optical imaging.

Because linear problems are easier and faster to solve than nonlinear problems, one may want to linearize, and thus simplify, an originally nonlinear model. The price to pay is an increased error in the reconstruction that is due to the decreased accuracy of the linearized model. Linearizing the banana-integral approach leads to the method described in later sections in this paper.

The general approach outlined above for devising and investigating reconstructive imaging methods has indeed partly been followed by the research community,[34,47,48] except that the third step described above is generally missing. However, as noted above, that step has already been done by others in related areas. The results of those investigations suggest that reconstructive optical imaging methods should in principle be possible, but with a poor resolution only. Therefore, despite the added time cost in these approaches, the resultant images are unlikely to be considerably better than the images that are obtained by our simple semiempirical approach discussed in the following several subsections.

B. Filtered Backprojection Tomography: Parallel Beams

As discussed in the sections above, the most probable paths of observed photons at a detector are confined to a narrow bananalike volume starting from the source. Therefore, in principle, as a first approximation, we can ignore all the diffusion and refraction effects present in optical projections and assume that we can treat these paths as if they were straight-line photon projections. With this simplified picture, we can attempt to obtain the blurred images of the study area by the techniques provided for x-ray CT.[49] Initial reconstructions with this approach have been described in a few of the recent studies.[13,50]

In this subsection, we first apply the x-ray filtered backprojection technique on the projections obtained in the sections above. In doing so, we ignore all the diffusion effects and nonlinearities in these projections. However, as a result, we at least get a first-order picture on which to base our following reconstruction techniques. In our definition, the zeroth-order image is the homogeneous diffuse medium assumption on the data that has been assumed to obtain a background attenuation value discussed in the Subsection 2.B.4. Following the simplistic application of the filtered backprojection technique, we then present a short discussion on some of the iterative techniques used for nonlinear image reconstruction both with optical projections and also in EIT and ultrasound diffraction tomography.

Note that, from the projections, the physical quantity of interest, the transmitted intensity, or the attenuation coefficient that we would like to image are given in the projection space (s, θ) as shown in Eqs. (21), (22), or (25). Because these quantities are not defined in the object space (x, y), we cannot obtain their images directly. In the filtered backprojection method, the image for the physical quantity of interest can be obtained by the use of an approach based on the inverse Radon transforms.[49] This is the inverse of the transform in Eq. (18) or (20) and is given by[42,49]

$$\kappa(x, y) = \int_0^{\pi} \int_{-\infty}^{\infty} \mathbf{F}^{-1}\{H(f_s)\mathbf{F}[\kappa(s, \theta)]\} \times \delta(x \cos\theta + y \sin\theta - s)\mathrm{d}s\mathrm{d}\theta, \quad (30)$$

or, simply,

$$\kappa(x, y) = \int_0^{\pi} \mathbf{F}^{-1}\{H(f_s)\mathbf{F}[\kappa(s, \theta)]\}\mathrm{d}\theta, \quad (31)$$

provided that the proper values of the parameter s are used for a given (x, y) and angle θ. In Eq. (31), $\kappa(s, \theta)$ is the projection data shown in Subsection 2.B and $\kappa(x, y)$ is the 2D image of the attenuation coefficient in the object space. $\mathbf{F}[\,]$ and $\mathbf{F}^{-1}[\,]$ are the forward and the inverse Fourier transforms, respectively. $H(f_s)$ is the Fourier transform of the $1/r$ filter function. In practice, this filter can have different forms including low-pass cosine and generalized Hamming. But for the simplest form we take a bandlimiting (RAM-LAK) filter defined by

$$H(f_s) = |f_s|\mathrm{Rect}\left(\frac{f_s}{2f_{s0}}\right), \quad (32)$$

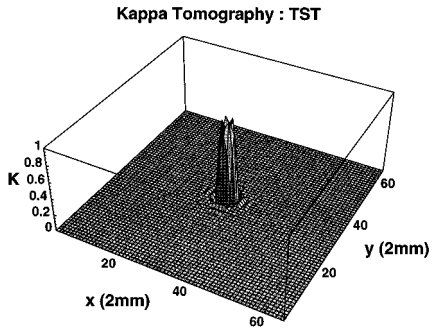

Fig. 20. Filtered backprojection tomographic image of the x-ray projection discussed in Fig. 13 for a cylinder of 5-mm diameter in transparent (TST) media.

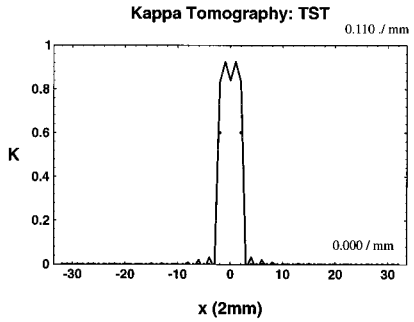

Fig. 21. Cross-sectional view of the tomographic image in Fig. 20. The numbers on the right axis give the maximum and the minimum quantitative values for this graph.

with a cutoff frequency f_{s0} located at half of the highest frequency sampled in the Fourier transform. In principle, in order for such filtering to work properly, one has to apply this operation to the tomography from a high number of homogeneously distributed projections.

The filtered backprojection integral given above is calculated by the transformation of the integral into a summation for each projection angle. The discrete projections are then fast Fourier transformed in s space and filtered by the $1/r$ filter and inverse fast Fourier transformed back to the s space. Note that each term in the summation has a distinct s and θ. Then for each (x, y) coordinate point, one can calculate the s coordinate for a given projection angle θ by using Eq. (16). Then one uses the available s coordinates of the real projections to interpolate the value of the attenuation coefficient by finding the range where s_{xy} lies in the interval (s_1, s_2). After this summation is completed for all projection angles θ, that is, for our examples from 0° to 180° in 1° steps, the resultant tomographic image of the attenuation coefficient is normalized. The normalization of the attenuation coefficients are defined similarly, as above [see Eq. (23)].

1. *Backprojection in Transparent Media*

In order to demonstrate the simplified backprojection approach, we first start with the reconstruction of the image of the object in a transparent medium with its projection given in Fig. 13. This projection is for an infinite cylinder with radius $r = 5$ mm and placed at the origin. Because the object is cylindrically symmetric, its projections at different angles θ will be the same. The surface plots on results of the filtered backprojection reconstruction are shown in Fig. 20. A cross section of this image through its center is given in Fig. 21. From the data in Figs. 13 and 21, we obtain the following quantitative conclusions. First, as expected, the diameter of the image is ~10 mm, which is in agreement with the starting value of $r = 5$ mm for this example. Second, the oscillations around the object are due to the sharp cutoff frequency of the $1/r$ bandlimiting filter. The absolute value of the peak attenuation coefficient in the cross-sectional image of Fig. 21 is obtained as follows. The integrated value under the surface of the normalized tomographic image is approximately $KXY = 70$ mm^2. The integrated absolute value of the attenuation coefficient can also be calculated from the original projection given in Fig. 13, assuming that the projection is spread over the whole distance L between the source and the detector. This gives a value of approximately $\kappa SL = 7.6$ mm. Therefore the peak of the final tomographic image for the attenuation coefficient must then be $\kappa_{max} = (\kappa SL)/(KXY) = 7.6/70 = 0.11$/mm. This value, within the noise limits of our crude approximation, is within 10% of the absorption coefficient used as input.

2. *Backprojection in Diffuse Media*

As mentioned above, as a first approximation, one can ignore the diffusion and refraction effects present in the optical projections and obtain the images of the object by x-ray CT methods. In order to demonstrate this, we use the intensity–attenuation coefficient projections studied in Subsection 2.B. To illustrate the technique of generating an image, we have chosen the most simple example of a cylinder placed at the origin, as described in that section. This area is probed by parallel-beam projections, also as described in Subsection 2.B. The optical coefficients and other parameters of the object space are summarized in Table 1. Because the object is cylindrically symmetric, its projections at different angles θ will be the same. The backprojection reconstruction algorithm used here is exactly the same as described in Eqs. (30)–(32). The results of an example reconstruction applied on data in Fig. 14 are shown in Fig. 22. A cross section of this image through its center is given in Fig. 23. From the data in Figs. 14 and 23, we obtain the following quantitative conclusions. First, the diameter of the image is ~28 mm (FWHM), which is much larger than the starting input value of $r = 5$ mm.

The absolute value of the peak attenuation coefficient in the cross-sectional image of Fig. 23 is obtained as explained above. This was described for the x-ray tomography in transparent media in Subsection 3.B.1. The integrated value under the surface of the normalized tomographic image is

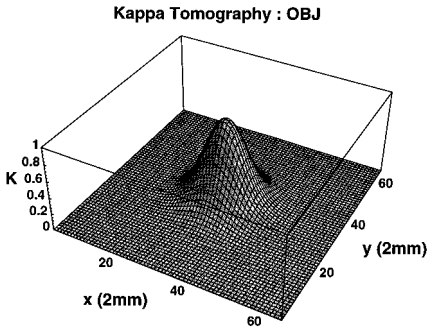

Fig. 22. Results of filtered backprojection tomography when effects coming from light diffusion in the attenuation coefficient projection data of Fig. 14 are ignored. The FWHM of the peak in the image is ~28 mm, and its peak is $\kappa_{max} = \kappa_0 + 1.1 \times 10^{-4}$ (1/mm), where $\kappa_0 = 0.174069$/mm is the background attenuation corresponding to the base at $K = 0$.

approximately $KXY = 615$ mm^2. Similarly, the integrated absolute value of the attenuation coefficient, from the original projection given in Fig. 14, is approximately $\kappa SL = 6.53 \times 10^{-2}$ mm. Therefore the peak of the final tomographic image for the attenuation coefficient must then be $\kappa_{max} = (\kappa SL)/(KXY) = 6.53 \times 10^{-2}/615 = 1.1 \times 10^{-4}$/mm. This value is much smaller than the peak attenuation constant difference of 8.64×10^{-4} used as input. This naturally arises from the broadening of the image that is due to diffusion.

Note that this indirect method to obtain quantitative values is used because it is difficult to keep track of the quantitative values during the processes required as defined by Eqs. (30)–(32). We have to process our reconstructed images in Fourier space with filtering operations. These make the quantitative calculations more difficult. As a result, in this paper our calculations with Eqs. (30)–(32) have been done on normalized quantities. The attenuation coefficient values calculated as we described above reflect an effective attenuation parameter that needs to be corrected because of multiple-scattering events in order to come up with the correct absorption coefficient.

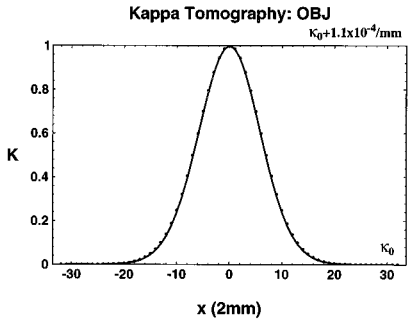

Fig. 23. Cross-sectional view of the tomographic image shown in Fig. 22. The half-width of the image is 28 mm (FWHM), which is much larger than the input object diameter, which is 10 mm. The numbers on the right axis give the maximum and the minimum quantitative values for this graph. These values are used in the text to compute contrast in the images.

We are making such a study aimed at these correction factors at this time. Another point is that, related to the same reason of multiple scattering, it is not obvious if the calculations described above would be applicable for cases in which the diffuse optical projections have a high amount of nonlinearities coming from strong objects that tend to screen each other or themselves. For such cases, in order to obtain absolute values, the set of Eqs. (30)–(32) has to be processed on quantitative parameters.

C. Optical Tomography in Diffusive Media: Parallel Beams

In Subsection 3.B, we assumed that the optical projections in diffuse media were taken as with x-ray-type projections, and we applied the standard filtered backprojection technique on it as a first-order guess of the object image. From the examples studied there, it is clear that a direct application of filtered backprojection tomography to the reconstruction of images of diffuse media will result in highly broadened and distorted images. We see that both the width and the strength of an object are in error in a reconstructed image with this technique. In this and the following sections, we describe semiempirical methods to compensate for these effects. These methods are based on simplified assumptions about the propagation of light in tissue. One can improve the quality of the image obtained with light-projection images by quantifying the blurring introduced by the diffusion of light. This information can be used to increase the resolution of the images by deconvolution in the Fourier space.[13] The effects coming from nonlinearities in the projections can be compensated for by nonlinear coordinate transformations. As we see below, these types of approaches lead to relatively simple and fast reconstruction algorithms based on deconvolution.

1. Backprojection Tomography with Deblurring

Deblurring of images of objects in diffuse media is achieved in the Fourier space by the deconvolving of the image in the object space by a blurring function. This blurring function, or the PSF, can be calculated approximately from the optical parameters of the diffusive medium. The calculations for such blurring, or Banana, functions were described in the sections above. Here we simply assume that we have a method to find an effective attenuation coefficient for the medium, which is the main determining factor for the width of the blurring diffuse medium.

In order to demonstrate our deblurring approach in the simplest way, we start with the same theoretical examples discussed in the sections above. We use the parallel-beam projection geometry in Fig. 8 with the medium–object parameters as given in Table 1, in which the object, which is defined as an optically diffusive infinite cylinder with radius $r = 5$ mm, is placed at the origin. As described above, we obtain the projections of photon density by using the PMI software package and then convert these into the attenuation coefficient κ. In Subsection 3.B.2 we as-

sumed that the attenuation coefficient projections were taken as with x-ray projections and applied the standard filtered backprojection technique. The results of such a first-order x-ray reconstruction are shown in Fig. 22.

Because this object is centered and its parameters do not differ much compared with those of the surroundings, we can use a single deblurring function that can be calculated from the peak attenuation coefficient observed from the projections. For this demonstration example, in order to test the limits of our deblurring procedure, we use a blurring function (or PSF) coming from the solution of the diffusion equation for a thin cylinder in a medium represented by the same optical coefficients obtained from the projections. The parameters of this thin cylindrical object are given in Table 1 in the column labeled Object—PSF. The projection of the same blurring function is shown in Fig. 11. We use this blurring function, or PSF, to deconvolve the image in the Fourier space from the transform of the image and the PSF. Although space-invariant deblurring is a simplified procedure, it still gives dramatically improved resolution for many cases because the width of the blurring function does not show large variations within the object space unless the point of interest is close to the source or the detector locations.

For our first example, because we demonstrate our approach with a space-invariant deblurring, we incorporate the deconvolution step mentioned above in the normal procedure of the filtered backprojection. In this case, the backprojection procedure described in Subsection 3.B by Eq. (31) is modified to give

$$K(x, y) = \int_0^{\pi} \mathbf{F}^{-1}\left\{H(f_s)\,\frac{\mathbf{F}[\kappa(s, \theta)]}{\mathbf{F}[\mathrm{PSF}(s, \theta)]}\right\}\mathrm{d}\theta, \quad (33)$$

where $\mathrm{PSF}(s, \theta)$ is the projection of the PSF. For the present example, it always has the same shape, regardless of the angle of the projection. Although we get these projections from a numerical solution, they are nearly the same as the shapes that are calculated from the simple banana function expression in Eq. (15). The result of these deblurred reconstruction steps applied on the projection of Fig. 14 is shown in Fig. 24. The corresponding reconstructed image without the deblurring step is shown in Fig. 22. As can easily be seen, the result is a dramatic improvement on the resolution of the image. However, we should note that this is only a simplified case of a centered weak object and its projections are not corrupted with noise, as is common in experimental data.

A cross section of this image through its center is given in Fig. 25. From the projection data in Fig. 14 and the image cross section in Fig. 25, we obtain the following quantitative conclusions. First, the diameter of the cylindrical object in the deblurred image is ~12 mm (FWHM), which is in good agreement with the starting input value for the radius of $r = 5$ mm. The absolute value of the peak attenuation coefficient

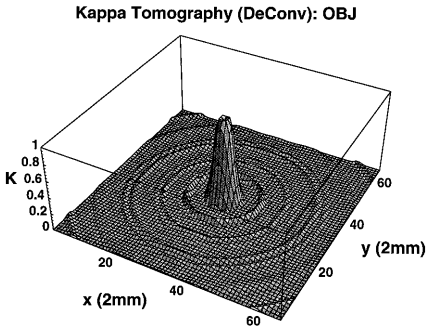

Fig. 24. Results of filtered backprojection tomography with a deconvolution (DeConv) step for correcting light diffusion in the image of Fig. 22. The FWHM of the peak in the deconvolved image is ~12 mm and its peak is $\kappa_{max} = \kappa_0 + 0.7 \times 10^{-3}$ (1/mm), where $\kappa_0 = 0.174069$/mm is the background attenuation coefficient that corresponds to the base of the figure at $K = 0$. These values agree well with the object parameters.

in the cross-sectional image of Fig. 25 is obtained as above. The integrated value under the surface of the normalized tomographic image is approximately $KXY = 90$ mm^2. The integrated absolute value of the attenuation coefficient, from the original projection given in Fig. 14, is already given above as $\kappa SL = 6.53 \times 10^{-2}$ mm. Therefore the peak of the final tomographic image for the attenuation coefficient must then be $\kappa_{max} = (\kappa SL)/(KXY) = 6.53 \times 10^{-2}/90 = 7 \times 10^{-4}$/mm. This value is also in good agreement with the peak attenuation constant difference of 8.64×10^{-4} used as input. The oscillations around the image of the object in Figs. 24 and 25 are due to the sharp cutoff frequency of the $1/r$ bandlimiting filter.

In summary, from Figs. 23 and 25, which correspond to the central cross-sectional profiles of the images before and after deblurring, respectively, we find that (1) an error of $\Delta r_{dB} = 1$ mm in the radius of the reconstructed object after deblurring to the error of $\Delta r_{org} = 9$ mm before deblurring corresponds to a resolution improvement of nearly an order of magnitude, and (2) by comparing the peak attenuation values $\Delta\kappa_{dB} = 7 \times 10^{-4}$/mm after deblurring and $\Delta\kappa_{org}$

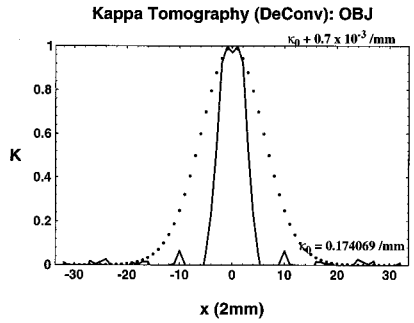

Fig. 25. Cross-sectional view of the tomographic image shown in Fig. 24. The half-width of the image is 12 mm (FWHM), which agrees well with the input object diameter, which is 10 mm. The numbers on the right axis give the maximum and the minimum quantitative values for this graph.

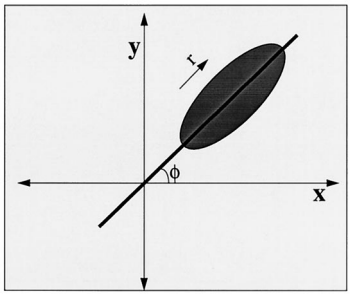

Fig. 26. Schematic illustration on the spatial dependence of the blurring function in the object space.

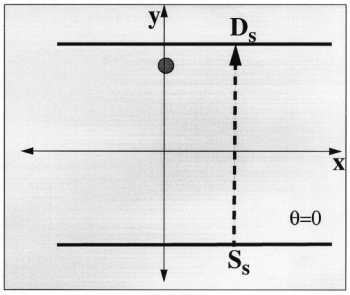

Fig. 27. Schematic illustration of the projection geometry for the example that demonstrates the spatially dependent deblurring process. A thin offset cylinder is placed in a turbid medium and imaged by two orthogonal projections. One of the projections (0° angle) is shown in the figure. The other is orthogonal to that at 90°.

$= 1.1 \times 10^{-4}$/mm before deblurring, we obtain a contrast improvement of a factor of ~7, obtained by the process of deblurring.

2. Spatially Variant Deblurring

The space-invariant blurring function described above can be used because the object is centered, is small compared with the image space, and its optical parameters differ by only a small amount from the background value. In this case, as indicated in the caption of Fig. 25, the radius and the magnitude of the inhomogeneity are imaged accurately after the deblurring step is incorporated into the backprojection technique.

In the object space, the blurring function or the PSF has two orthogonal parameters describing its width. One of these is along the radial direction s with respect to the center, and the other is along the projection angle ϕ direction. For the parallel-beam projection geometry, the variation in radial (along s) width of the blurring does not exist because of identical projection distances for each source–detector pair. However, the width of the blurring shows an angle (along ϕ) dependence as one moves in the radial direction. At exactly the center of the object space, the PSF is round and gets more and more elliptical when one decreases its size in the ϕ direction as one moves radially out. This blurring function distortion as function of spatial position away from the center is shown schematically in Fig. 26. This spatial dependence is a direct consequence of the variation in the banana function width shown in Fig. 6. As a result of this, for proper deblurring of images, one has to take this spatial dependence into account. This is discussed next. Note that, in the discussion given above, we ignored the variation that is due to the magnitude of the weight function near the source–detector positions, as shown in Fig. 4.

One of the ways to handle the radial dependence of the deblurring function is to apply the deblurring operation after the image has been transformed into the cylindrical coordinate system. In this system, the convolution can be done in two steps. The first is to deconvolve in the radial direction with a banana function that corresponds to the position halfway between the source and the detector. The second is to deconvolve in the angular ϕ direction with a radially dependent banana function. In our numerical studies, we have found that the separability of the blurring function into a radial and an angular component is a good approximation.

One can compute the radial dependence of the banana function discussed above from the expression in Eq. (15) by taking the radial distance variation along the x-axis direction. Similar approaches have already been applied in the restoration of medical images taken by CT[25] and EIT.[18] This approach is discussed in detail in Subsection 3.D, in which we describe our reconstruction technique for the fan-beam projection geometry. Here, for demonstration purposes, we apply a spatially variant deblurring process to obtain images of a thin cylinder from the simplified example of only two orthogonal projections. The parameters of the cylinder and the turbid medium are identical to the parameters given in Table 1, with two exceptions. The first is that the radius of the cylinder is 2 mm, and the second is that we place the cylinder off set from the center on the y axis 45 mm away from the origin. Two orthogonal projections are taken. One is along the x axis, leaving the object midway from the source–detector lines. The other is along the y axis, in which case the object is 5 mm away from the detector line and 95 mm away from the source line. This geometry and the y-axis projection are schematically indicated in Fig. 27.

The projections corresponding to the geometry given in Fig. 27 are computed numerically from the solution of the diffusion equation for the optical parameters given in Table 1. The results for the two orthogonal projections are shown in Fig. 28. The dotted curves in this figure are two banana functions calculated as described below. The first-order image found from these two projections is shown in Fig. 29. Because we have only two projections, we have used the multiplication of the values of the projections for each spatial point in (x, y) space rather than the summation in conventional backprojection. Specifically, we have used

$$\kappa(x, y) = \kappa(x, \theta_{00})\kappa(y, \theta_{90}), \tag{34}$$

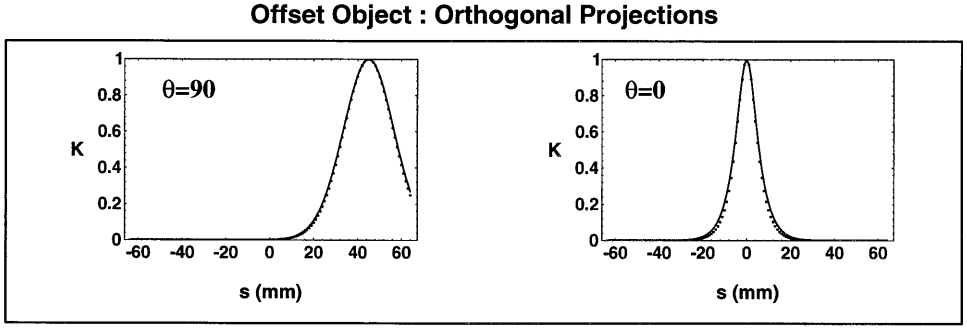

Fig. 28. Normalized attenuation coefficient K projections that correspond to the thin offset cylinder geometry described in the diffuse intensity projection in Fig. 27. The optical parameters are given in Table 1. Parallel-beam geometry is used for obtaining the optical projection image of the object. The object is an infinite cylinder offset from the origin $r = \{0, 45, 0\}$ mm. The dotted curves correspond to the two banana functions calculated by assuming an object–source (or –detector) distance found from the peak of the first-order image, which is discussed below.

where θ_{00} and θ_{90} indicate the two orthogonal projections at 0° and 90°, respectively. For the same reason of having only two projections, a filtering operation was also omitted because it would give worse distortions for the present case with two projections. However, because these reconstruction operations were applied identically to both the original and the deblurred tomographic images, the conclusions we make on the resolution improvements with deblurring process below remain valid. In order to compare the original images of an offset object with those of a centered object with identical parameters, we also give the first order image of a centered cylinder in Fig. 30. This latter image of the centered object is also obtained from only two orthogonal projections.

In order to deblur these images, the projections were deconvolved with the two deblurring banana functions, shown by the dotted curves in Fig. 28. We calculate these two banana functions by assuming an object–source (or –detector) distance that is found from the peak in the first-order image shown in Fig. 29. These distances are 50 and 5 mm for the two directions of the broadening in the imaged shape of the object. Therefore these deblurring banana functions take the spatial dependence of the broadening into account (see Fig. 28). The attenuation coefficient value needed for the calculation of these functions is taken to be $\kappa_0 = 0.180$/mm, which is also calculated from the projections themselves, as described above.

The fast Fourier transforms (FFT's) of the object projections and the deblurring functions (PSF's) are shown in Fig. 31. It is easily seen that if the spatial dependence of the blurring were not taken into account, a single deblurring function could not be used to deconvolve the object projections. Following the deconvolution of the projections with the corresponding deblurring functions, the second-order image is obtained by exactly the same process used to obtain the first-order image shown in Fig. 29. The results are shown in Fig. 32. In order to compare these deblurred images with those of a centered object, we also give the second-order image of a centered cylinder in Fig. 33.

From the deblurring results described in Figs. 32 and 33 compared with those of the corresponding original reconstructed images in Figs. 29 and 30, we conclude that, for noise-free measurements, one can in principle reconstruct the image of a point object in diffuse media. This obviously applies to the cases in which the objects are weak and there are no nonlinearities in the projections. In the case of nonlineari-

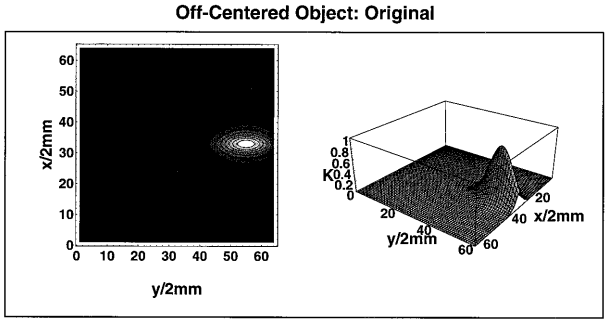

Fig. 29. Contour and surface plots of the tomographic first-order (no deblurring) image of the offset cylinder with the projections shown in Fig. 28. Only two projections are used.

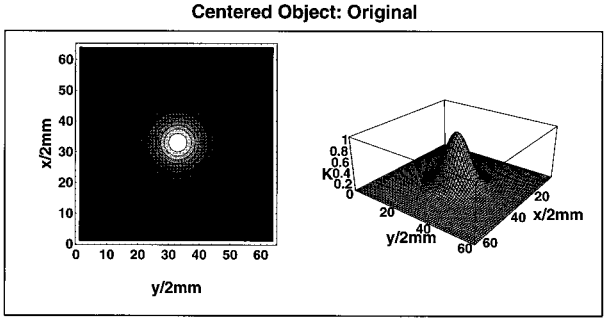

Fig. 30. Contour and surface plots of the tomographic first order (no deblurring) image of a centered cylinder with identical properties as those discussed for the offset cylinder. Only two projections are used.

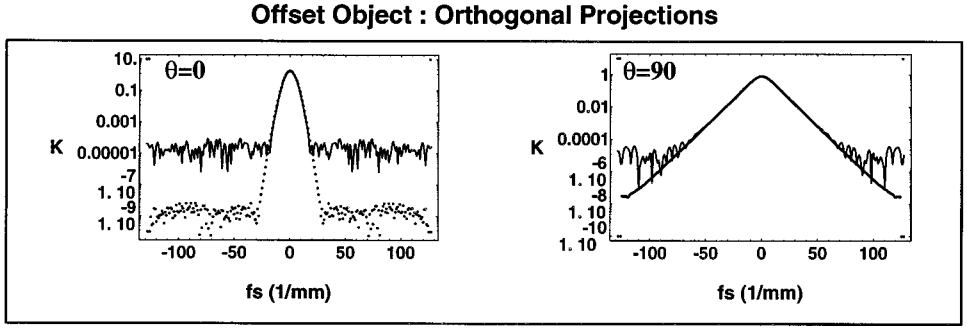

Fig. 31. FFT's of the attenuation coefficient K projections given in Fig. 28. The dotted curves correspond to the FFT's of the two banana functions shown in the same figure. We calculated these banana functions by taking the spatial dependence of the broadening.

ties, one has to apply correction for the bending of the statistical ray paths defined in the banana function. This is discussed next.

3. Nonlinearities

In the paragraphs above we have applied a deconvolution technique to deblur the optical projection images of objects in diffuse media. We have done this also by emphasizing the spatial dependence of the deblurring needed within the image space. However, there we have considered only objects with optical constants slightly different from those of the surrounding media. These objects are considered only weak perturbations. In this subsection we consider the effects of strong objects on the projections and on the deblurring process in the tomographic reconstruction.

If there is a large difference between optical constants of the object and the surrounding medium, then there are several physical factors causing nonlinearities in the projections. The meaning of this is simply that, as the strength of an object is increased, or if more and more objects are incorporated into the medium, their individual projections and the corresponding images do not add up in a linear fashion. On the contrary, a strong object tends to screen itself, and different objects tend to shade each other. These physical reasons are discussed further below.

Another obvious reason for the nonlinearity in the projections comes from the transformation between the intensity and the attenuation constant projections. The line shapes of intensity and attenuation constant projections should be different because of the exponential relationship between these two quantities. This exponential transformation causes the normalized attenuation constant projections of strong objects to be narrower than those for the weak objects, even if their light intensity projections have identical normalized shapes. There are two solutions to this. One is to apply the deblurring process in the intensity image rather than in the attenuation image. The other correction method, which is the one actually used below, is to apply the same nonlinear transformation to either the banana function or to the attenuation projection shape, according to the strength of an object in the image space.

As a result, optical imaging from projections is basically a nonlinear process. Because our deblurring method uses deconvolution in images transformed into Fourier space, it is applicable to only linear im-

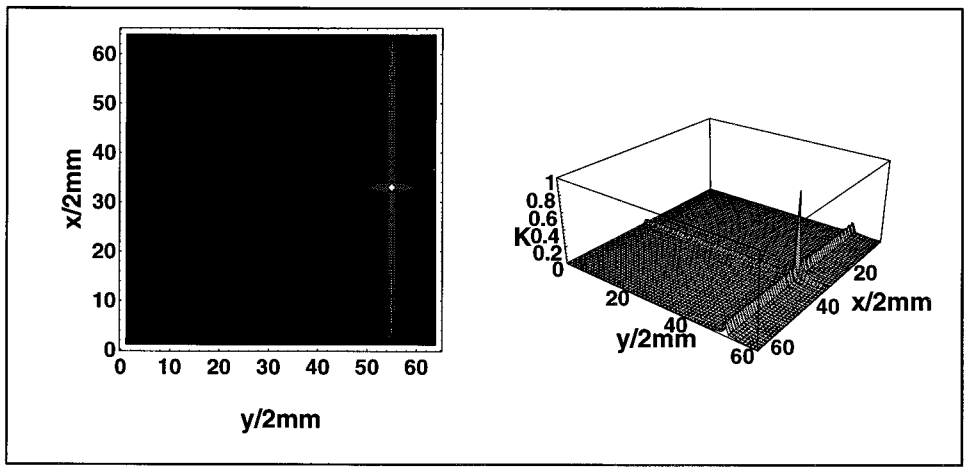

Fig. 32. Contour and surface plots of the tomographic second-order deblurred image of the offset cylinder with the projections shown in Fig. 28. As can be seen from the comparison of this image with the one shown in Fig. 29, the resolution has improved dramatically.

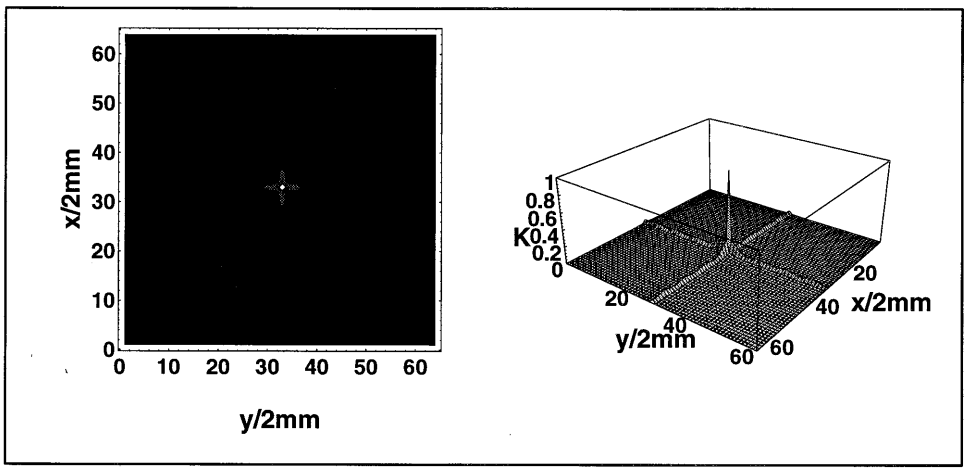

Fig. 33. Contour and surface plots of the tomographic second-order deblurred image of the offset cylinder with the projections shown in Fig. 28. The resolution has improved dramatically in comparison with the one shown in Fig. 30.

ages. Therefore, for strongly perturbing objects, one has to apply this method with appropriate precautions, which is the topic of this subsection.

As already mentioned above briefly, the main reason for the nonlinearities comes simply from the physics of light propagation in optical media and especially because of the statistical nature of this propagation in diffuse media. If there is a large optical difference between the object and the surrounding medium, then the object tends to warp the paths of the light rays around it. In other words, the density of the light rays tends to become distorted and bent, compared with the banana profiles shown in Fig. 6. Because of this effective warping of the space with respect to the straight projection geometry, the projections of strongly perturbing objects are different from those that correspond to weakly perturbing objects. This is a simple consequence of the statistics of the photons trying to reach from the source to the detector with the minimum amount of attenuation. As the object gets stronger, the survivor photons that can reach the detector are those that take a longer path than before because they are pushed away from the absorption of the object. This is schematically illustrated in Fig. 34. The result of this is demonstrated in Fig. 12 for the intensity projections of strong (solid curves) and weak (dotted curves) objects. It is clearly seen in this figure that, as the object gets stronger, its projection gets wider, whether it is centered or not.

Another related effect that is due to the nonlinearities of projection-image formation is that, as the photons propagate and diffuse from the source to the detector, they experience significantly different blurring parameters near strong objects as compared to the case with the background medium alone. They also remember this experience, and the total blurring within a projection image is an accumulated effect of

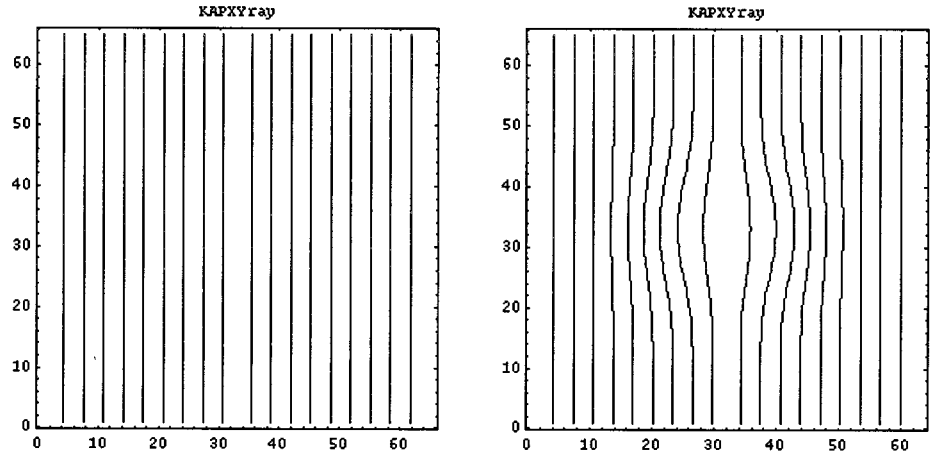

Fig. 34. Projection ray paths probing a media with a weakly absorbing cylinder (left) and a strongly absorbing cylinder (right). These are calculated semiempirically by the replacement of the refractive-index inhomogeneity term in the geometric ray equation with the attenuation constant changes. The distortions that are due to the strength of the object on the right are clearly visible, and these affect the shape of the bananas that are used to deblur the image.

all the objects encountered in their paths. For the simple case of one object, illustrated in Fig. 34, the blurring function is narrowest near the object, becomes wider, and approaches the shape of the blurring function of the background medium as one moves away from the object. Therefore, in order to be able to apply a deblurring process that depends on a single banana function, one has to expand the shape of the image near the strong object.

As the intensity projections of stronger objects are wider, they should also propagate into the normalized attenuation constant projections, widening them as well. However, such a widening may not be enough to correct for the narrowing in the attenuation projections because of the exponential relationship between intensity and attenuation mentioned above. In fact, the normalized projections in Fig. 16 show that the attenuation projection profile of a strong object (curve b) is considerably narrower than that for the weak object (curve a). Because the attenuation constant of the strong object has a narrower projection image than the corresponding one for the weak object, one can not apply the same deblurring function to the strong object image as was done for the weak object. One must either find a proper deblurring process for this nonlinear image or transform the image so that it can be deblurred with the same function. We first attempt to do the latter in an empirical way based on the physical reasoning discussed in the paragraphs above. Note that, even for reconstruction from nonlinear photon density images as defined in Fig. 12, in which serious mathematical problems would not arise, the deblurring process would not work with optimal effectiveness.

From the discussion above, we already know that the effect of the strong attenuation constant is to push away and distort the statistical paths of the photons propagating around it. We expect that the amount of distortion is related to the perturbed density of the photons that reflect the strong nearby attenuation. In order to translate this effect in terms of coordinate transformations, we approximate the relationship of the image-space radial coordinates x to perturbation photon density $\varphi_1(x)$ by

$$x = r + C_e \frac{\mathrm{d}}{\mathrm{d}x} \varphi_1(x), \tag{35}$$

where r is the distance in the real space if distortions are corrected and C_e is a constant that is estimated empirically below. An estimate of the real $\varphi_1(x)$ is assumed to be given by the first-order image of the object. A plot of this transformation is given in Fig. 35. Note that the distorted image has to be expanded near the center in order to compensate for the distortions that are due to nonlinearities. Furthermore, the location of the center of the object in the distorted projection space x and the real space r is the same. Applying this expansion on the intensity projection image of the strong object indicated by curve b in Fig. 12 would broaden that projection, which in turn would also broaden the attenuation coefficient

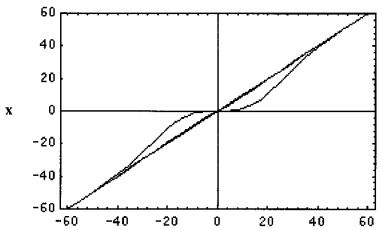

Fig. 35. Coordinate transformations used to compensate for the effects of ray-path bending demonstrated in Fig. 33.

projection. We further note that this is an operation needed to be able to apply a single deblurring step to this projection. The only trouble is that at this time we do not have any theoretical means to estimate the exact magnitude of the coordinate transformation or the magnitude of the constant C_e discussed above. Our discussion above has been based on purely qualitative and empirical concepts. Therefore we can also estimate the magnitude of this constant empirically, as described below.

The percentage difference in the line shapes of the attenuation coefficients for the weak and the strong objects are plotted in Fig. 36. Note that the qualitative shape of this difference is identical to that of the coordinate transformations discussed above, that is, the conclusion from Fig. 36 is that the coordinates of the center of the object remain the same; the coordinate region immediately next to the center has to be expanded to give the indicated amplitude increase. Although, because of scaling problems, it is not apparent from Fig. 36 that the regions far from the center are shrunk. This is the same behavior shown in the slopes of the transformation in Fig. 35. Therefore, by using a coordinate transformation, as indicated in Fig. 35, that corresponds to a constant C_e such that the resultant shape changes are quantitatively the same as those shown in Fig. 36, we end up with a corrected image that can be deblurred in a similar fashion as the weak object, which was deblurred previously in this subsection.

After obtaining the object image in the transformed coordinate system with the right magnitude found empirically, we then can use a single PSF to decon-

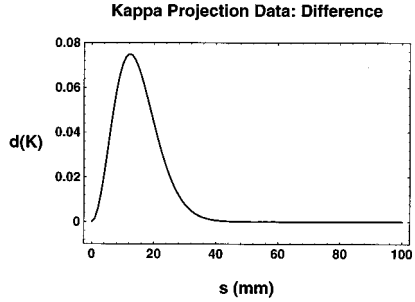

Fig. 36. Strongly absorbing cylinders distort the projection rays around themselves and result in the indicated difference compared with a weak cylinder. This curve gives the difference between curves a and b in Fig. 16.

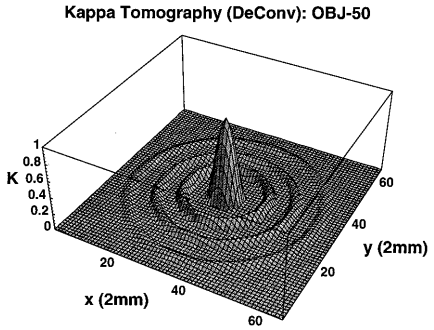

Fig. 37. Results of filtered backprojection tomography for a strong object with an absorption coefficient 50 times higher than that of the background medium. This object is identical to the one discussed in Fig. 24, except that the absorption coefficient of the object in Fig. 24 is only 1% higher than that of the background medium. Despite this difference in the strengths of these objects, the reconstructed image above, which applies deblurring and coordinate transformations to compensate for diffusion and imaging nonlinearities, respectively, is of comparable resolution with that of the image of the weak object shown in Fig. 24. The FWHM of the peak in the deconvolved image above is still ~12 mm but its shape is rounded because of the additional filtering needed to decrease the effects of noise in the projections processed further for coordinate transformations.

volve the image in the projection space, as this object is centered. As discussed above, this could be done because the object is small compared with the image space. The results of this reconstruction technique, including the corrections for imaging nonlinearities by coordinate transformations, result in the image shown in Fig. 37 as a surface plot. The cross section of this image is shown in Fig. 38 and is compared with the width of the original image without deblurring or refraction corrections.

D. Backprojection Tomography in Diffuse Media: Fan Beams

1. *Radially Dependent Blurring*

As discussed above for the parallel-beam geometry, the projections in diffuse media are broadened by an amount determined by the optical constants of these media. The amount of broadening is also a function

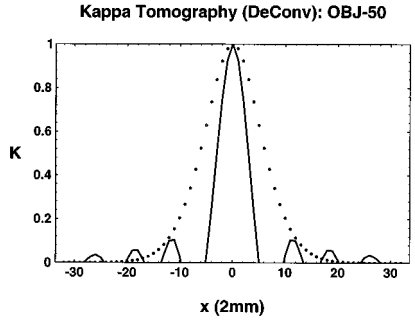

Fig. 38. Central cross section of the reconstructed image shown in Fig. 37. The profile of the image without deblurring is also indicated by the dotted curve for comparison.

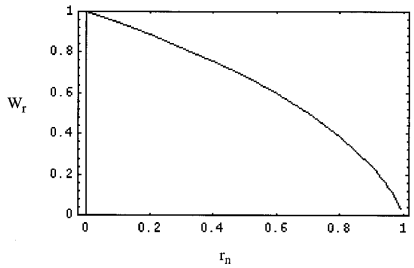

Fig. 39. Radial dependence of the width of the blurring function along the radial direction in the fan-beam tomography geometry. This is calculated from the dependence of the width of the banana function as a function of the source–detector distance for typical diffuse medium parameters.

of the location of the object as illustrated for the case of parallel-beam projections. The blurring function has two width parameters (see Fig. 26). One is along the radial and the other is along the projection angle direction. In the parallel-beam projection case, we incorporated the spatial dependence of the angular width of the blurring function. In the fan-beam case, there is one additional spatial dependence, that is, as the source–detector points get closer, the banana width decreases; the effects of this appear as a radially dependent width of the blurring function along the radial direction as well. This radial dependence of the normalized width of the blurring function along the radial direction is illustrated in Fig. 39. From this figure it is clear that the broadening is greater if the object of interest is placed at the center of the object space in the fan geometry.

Figure 26 shows that the blurring function has an elliptical FWHM contour in the cross section, which is also true for the fan geometry. This is naturally correct only in the absence of strong inhomogeneities. From this, we immediately see that, for a given constant r, the blurring function does not depend on the angle ϕ. However, for a constant ϕ, both the radial and the angle dependences of the FWHM of the blurring function have a strong dependence on the radial distance. We take these effects into account as we process our data below for tomographic image reconstruction.

One of the easiest ways to handle the spatial dependence of the deblurring function is to use a radial coordinate transformation to compensate for this spatial variation. Such approaches have already been applied in image restoration for general applications[28] and, as mentioned above include medical images taken by CT[25] and EIT.[18] With such a coordinate transformation we basically would like to achieve an expansion of the space coordinates at large radial distances relative to the space at small radial distances. The coordinate transformations necessary for this are shown in Fig. 40 and correspond to the blurring width dependence given in Fig. 39. In Fig. 40, the radial expansion $\Delta r_n'$ ($= \mathrm{d}r_{\mathrm{new}}/\mathrm{d}r$), which is necessary at different normalized radial positions r_n for equalizing the blurring process, is shown. To achieve such a transformation, it is best

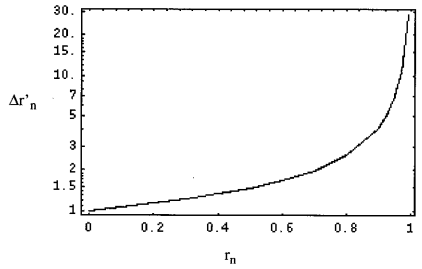

Fig. 40. Coordinate transformation for radial dependence of the deblurring. The radial expansion $\Delta r_n'$, which is necessary at different normalized radial positions r_n for equalizing the blurring process, is shown.

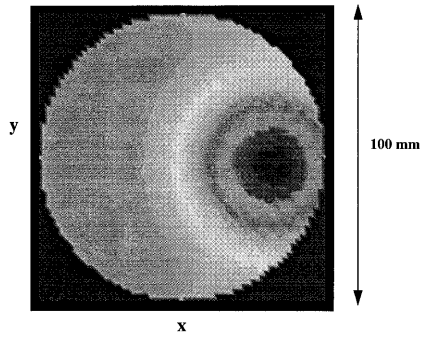

Fig. 41. Tomographic image of the cylindrical object with the x-ray backprojection tomography in the (x, y) Cartesian coordinate system. This is obtained by transformation from Fig. 42.

to work with the version of the image transformed from the (x, y) Cartesian coordinate space to the (r, ϕ) cylindrical space with expanded radial coordinates. After such a coordinate transformation, the image is Fourier transformed and divided by the Fourier transform of a single (space-invariant) deblurring function (PSF) that is also transformed into the cylindrical space.

2. *Backprojection with Fan Beams*

As above, as a first approximation, one can ignore all the diffusion and refraction effects present in optical projections and attempt to obtain the images of the study area by the techniques provided for x-ray CT. In order to demonstrate this, we use the set of numerical data discussed above. The procedure of backprojection tomography is based on Eq. (31).[42,49] Note that we could, in principle, follow the reconstruction of the image with this backprojection formula by applying it to the fan-beam projections transformed into the (s, θ) space. This, however, may result in reconstruction artifacts that are due to the inhomogeneous distribution of the s coordinates of the projections. Therefore we simplify the above backprojection integral by transforming it into a summation over the images obtained by projections for each source position in the fan-beam geometry, that is, we perform the integration and summation in the (i_S, j_D) space rather than in the (s, θ) space. Because in this space the filtering by the $1/r$ filter is not straightforward, we ignore it for the time being. For biological tissue imaging, the broadening that is due to the $1/r$ effect can be ignored, compared with the blurring that is due to optical diffusion effects.

In detail, the reconstruction is done as follows. The filtered backprojection integral given above is calculated by the transformation of the integral into a summation for each source index. Note that each term in the summation has a distinct i_S and j_D that correspond to a distinct set of source and detector coordinates $r_S = (x_S, y_S, z_S)$ and $r_D = (x_D, y_D, z_D)$, respectively. These coordinates define a line in the form of $y = a_{SD}x + c_{SD}$ for each source–detector pair. Then for each (x, y) coordinate point, one can calculate the pair of source–detector lines between which this coordinate point sits for a given source index i_S in the unfiltered backprojection example. After this, the distance of this (x, y) point to these two boundary lines are computed and used as weights for interpolation of the $K(x, y)$ value from the $K(i_{S1}, j_{D1})$ and $K(i_{S2}, j_{D2})$ values corresponding to the source–detector pairs whose lines are bounding the (x, y) point of interest. After this summation is completed for all projections corresponding to all sources, the resultant tomographic image of the attenuation coefficient is normalized. The normalization of the attenuation coefficients is done as defined above.

The results of such a reconstruction is shown in Fig. 41 for the (x, y) Cartesian coordinate system. This image is obtained by transformation from the (r, ϕ) cylindrical coordinate system image shown in Fig. 42. The use of the cylindrical system in the fan-beam projection geometry comes from the fact that the blurring function for the homogeneous object space can be approximately decoupled into radial- and angle-dependent parts that can be handled easier for deblurring in this coordinate system.

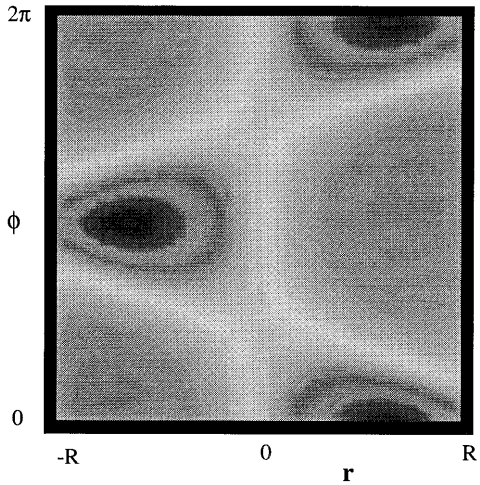

Fig. 42. First-order tomographic image of the cylindrical object with the x-ray backprojection tomography (r, ϕ) in the polar coordinate system.

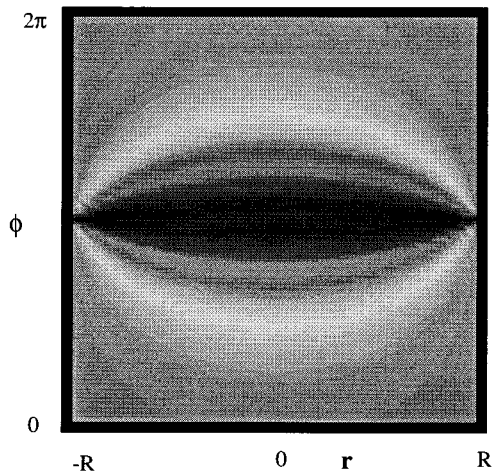

Fig. 43. Deblurring function used to deconvolve the first-order image along the ϕ direction. As discussed in the text, this is only an approximation to the real PSF because it ignores many of the additional corrections necessary in the fan-beam geometry.

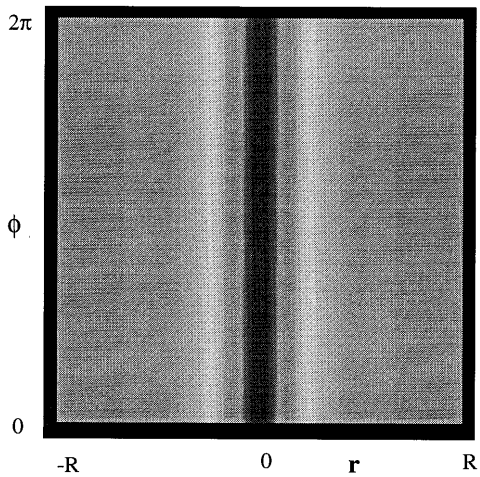

Fig. 44. Deblurring function used to deconvolve the first-order image along the r direction. Because of the radial coordinate transformations discussed in Fig. 40, a PSF with a single width is sufficient in the radial direction.

3. Deblurring

Deblurring in the fan-beam geometry is achieved in the Fourier space by the deconvolving of the image by a blurring function, which is calculated approximately from the optical parameters of the diffusive medium. The calculations for the attenuation constant that define these blurring or banana functions are described in the sections above.

Deblurring is done in the (r, ϕ) cylindrical coordinate system because of the spatial dependence of the blurring function described above. The procedure is as follows. After the first-order image of the object has been obtained in the (r, ϕ) coordinate system, as shown in Fig. 41, this image is transformed into the Fourier domain and deconvolved with the banana function profiles along the angular and the radial directions separately. The banana functions that approximate the PSF for these directions are shown in Figs. 43 and 44 for the angular and the radial directions, respectively. Note that these PSF profiles, especially the angular one, are only approximate because we have ignored effects such as the imaging nonlinearities, $1/r$ blurring, and image distortions that are due to the anisotropic angular distribution of the projections with respect to any arbitrary point.

The whole procedure of deblurring is illustrated in Figs. 42–45. The deblurred image in the polar system shown in Fig. 45 is then again transformed into the (x, y) coordinate system to have the final deblurred reconstructed image. As a result of these processes, we obtain the deblurred image given in Fig. 46. The original reconstructed image before deblurring is given in Fig. 41 with the same color coding for comparison. Note that the image of the object, shown by the darkest area on the right, is narrowed considerably to represent the size of the real object more correctly. The radial and the angular dependences of the deblurring, however, do not seem to work with equal success. This is most probably due to the approximations involved in separating the blurring function into two orthogonal components. We are currently studying this separability of these functions and the effects of the nonlinearities and the $1/r$ blurring mentioned above. The results of these studies and the quantitative performance of the deblurring process in the fan-beam geometry will be reported in detail later in a separate paper.

4. Optical Tomography in Diffuse Media: Experimental

In this section we present preliminary results on the application of our reconstruction method to the experimental data taken with both parallel-beam and fan-beam geometry. These results are preliminary in the sense that many of the procedures described above with theoretical data are now affected by the noise in the experimental data. As we describe below, some of

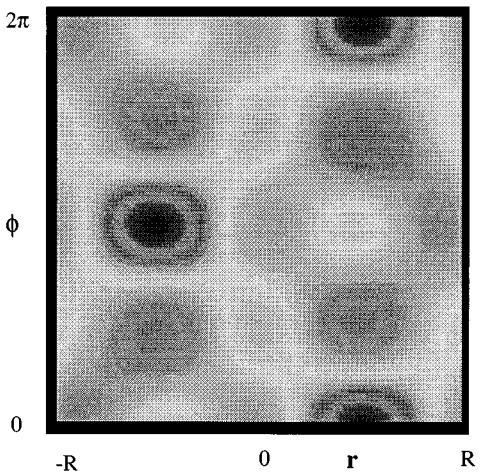

Fig. 45. Second-order deblurred tomographic image of the cylindrical object with the x-ray backprojection tomography in the (r, ϕ) polar coordinate system.

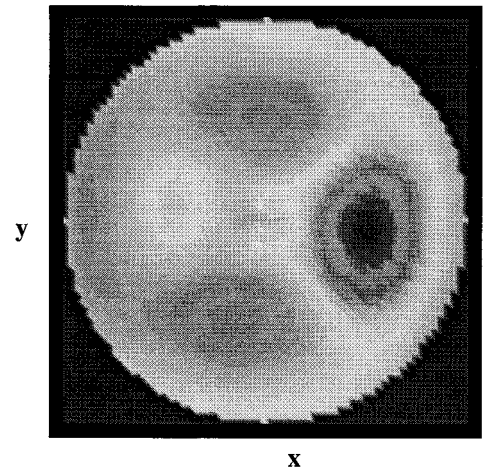

Fig. 46. Second-order deblurred tomographic image of the cylindrical object with the x-ray backprojection tomography in the (x, y) Cartesian coordinate system. This is obtained by transformation from Fig. 45. A comparison of the contours of the different gray levels in this figure for the deblurred image and the image in Fig. 41 before deblurring demonstrates the improvement in resolution in this geometry. The same color coding is used in both figures.

the sources for this noise, such as those coming from the practical limitations on the number or angle of projection views around the object, can in principle be avoided in well-designed professional tomographic systems. Nevertheless, currently we are still in the process of trying to optimize our techniques in order to decrease the effects of such noise sources by both experimental and mathematical means. Therefore many of the performance improvements in our deblurring process that are discussed below are limited primarily by the amount of noise, whether it is avoidable or not. The amount of noise, basically, puts a limit on the cutoff frequency on the usable Fourier components of the image. This is simply an outcome of the smoothing property of imaging in diffuse media discussed above. Because of these reasons, in this paper we do not go into any details on the performance limits of our procedures in experiments. The results below are presented simply as a set of preliminary demonstrations of our technique on experimental data. As is seen below, even for this preliminary set, the contrast and resolution improvements in images with the deblurring process discussed above are apparent. Considering the ease and the simplicity of the reconstruction technique used to obtain these effects, the observed improvements come at no additional cost compared with the difficulties in obtaining similar, if at all possible, improvements by experimental techniques such as ballistic photon imaging or photon density wave imaging.

A. Parallel-Beam Tomography with Phantoms

1. *Experimental Setup*

The main set of experiments was performed in parallel-beam projection geometry by the use of Delrin cylinders embedded in a tank of intralipid solution. Semiconductor injection lasers in the NIR with output powers of the order of 10 s of milliwatts were used as light sources. The geometry of the experiments and the optical parameters of the objects and the intralipid medium are given in Fig. 47. As seen in this figure, the projection measurements were done for only four sides of a square, that is, for $\theta = \{0°, 90°, 180°, 270°\}$, in order to minimize the experimental effort. As discussed above, this obviously limits the quality of the reconstructions. However, the results given below still demonstrate the potential gains in the image resolution that could be achieved by simple corrections for the light diffusion. Several examples of tomographic image reconstructions by the use of the parallel-beam geometry were presented earlier.[13] Here we examine primarily our recent experimental cases, including a 2D reconstruction of a complex object composed of four different cylinders with differing optical properties and a 3D reconstruction of an irregularly shaped object.

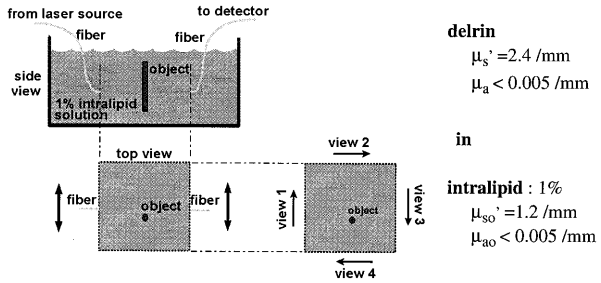

Fig. 47. Geometry of the parallel-beam projection experiments with Delrin cylinders in an intralipid solution.

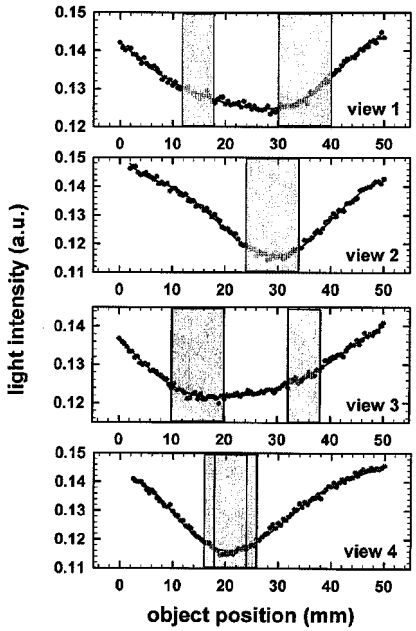

Fig. 48. Optical projection images of two Delrin cylinders with 6-mm- and 10-mm-diameters embedded in an intralipid solution. The real profiles and positions of the objects are indicated schematically as shaded areas. The projections are taken from four angles corresponding to the views from 0°, 90°, 180°, and 270°.

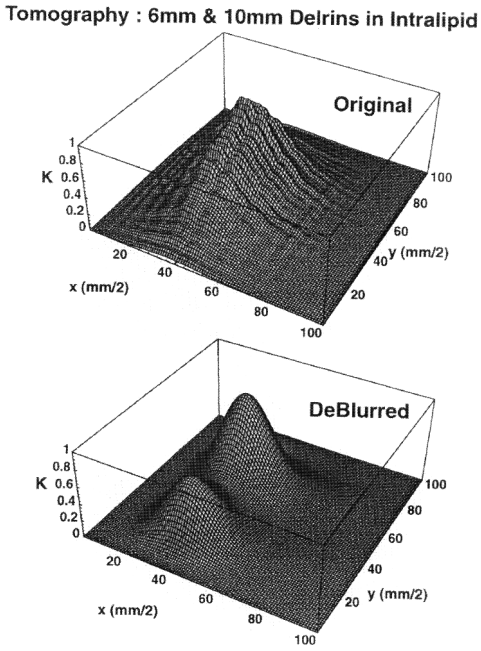

Fig. 49. 2D surface plots for the reconstructed slice image of the double object sample with 10-mm- and 6-mm-diameter Delrin cylinders embedded in the center of a 1% intralipid solution tank. The projections of the object are given in Fig. 48. The original image is shown on the top, and the deblurred image is shown on the bottom of the figure. The deblurring process resolves the two objects clearly. The profiles of these objects, however, are highly smoothed because of the large amount of noise present in the experimental data.

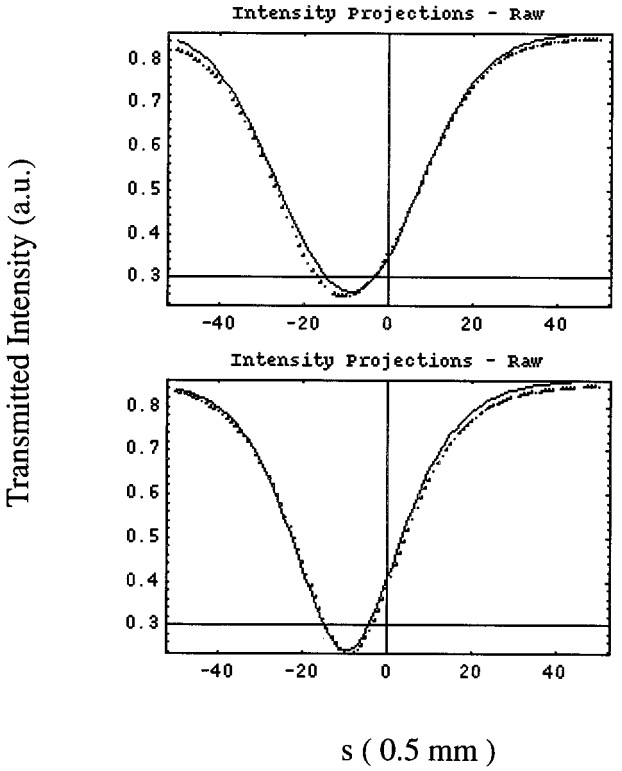

Fig. 50. Projections of a complex object composed of four cylinders with different optical properties. This composite object consists of two strongly absorbing cylinders (blackened metallic wires of ~1-mm diameter) and two weakly scattering larger diameter cylinders (Delrin cylinders of 6-mm and 10-mm diameters). Note that the projections do not reveal any internal structure of this complex object. The dotted and solid curves correspond to projections taken from opposite sides.

2. *Two Scattering Objects*

In the experimental geometry discussed above we placed two scattering Delrin cylinders of 6-mm and 10-mm diameters. The optical parameters of these objects are given in Fig. 47. The cylinders were placed ~20 mm apart from each other, and the line passing through their centers was ~5 mm away from the center of the projection area. The projections of these objects from the four sides of the square object space are shown in Fig. 48. The backprojection reconstructions with and without deblurring, as described in this paper, result in the surface images given in Fig. 49. The deblurred image clearly reveals the two individual peaks coming from the two scattering cylinders, whereas the original backprojection image shows a single broad peak. This result shows that a scattering coefficient contrast ratio of ~2 can be processed with our deblurring method to reveal the objects in more detail. We do not attempt to quantify the improvements in the image any further simply because such an analysis would hardly reveal the performance of our reconstruction under the limitations in the number (four) of views available to us at this time.

3. *Two Strong Objects Next to Two Weak Objects*

In the experimental geometry discussed above we placed a complex object composed of four cylindrical objects glued onto each other. Two of these were anodized (black) metal wires of ~1-mm diameter, and the other two were two Delrin cylinders of 6-mm and 10-mm diameters. These Delrin cylinders were identical to those described in the paragraph above. The optical parameters of the Delrin objects are given in Fig. 47, whereas the optical parameters of the blackened metallic wires are not known, other than the fact that they seem to provide an absorption contrast ratio of at least a couple of orders of magnitude. In other words, the metallic objects can be classified as two very strongly absorbing objects. The projections of these objects from the four sides of the square object space are shown in Fig. 50. Note that all these projections are nearly symmetric, single-peaked profiles. They result in a first-order reconstructed image that is a single, nearly isotropic broad peak. The backprojection reconstruction with deblurring described in this paper results in the surface-plot image given in Fig. 51. There have been no corrections for the effects of nonlinearities in this reconstruction to correct for the strength of the blackened wires with respect to the Delrin cylinders, which provide a weakly scattering contrast in the medium. The cross sections through this image are shown in Fig. 52, which clearly reveals the two individual peaks coming from the two strongly absorbing

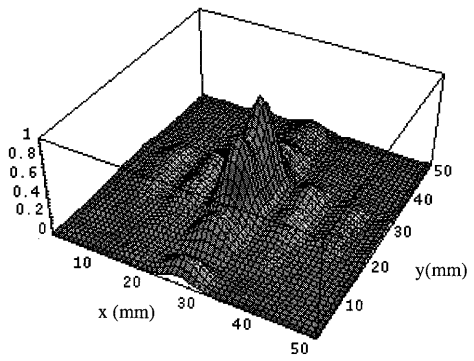

Fig. 51. Surface plot of the deblurred reconstructed image from the projections shown in Fig. 50. Deblurring helps to identify the two peaks coming from the two blackened metallic wires. However, the two Delrin cylinders are not resolved because of the screening effects of the high absorption contrast of the metallic wires. No corrections for imaging nonlinearities were applied.

metallic cylinders. In contrast to the results discussed in the previous paragraph, the weakly absorbing Delrin cylinders are not visible. This is obviously due to the strong perturbations of the wires screening the weak scattering contrast of these Delrin cylinders. We are in the process of applying corrections for nonlinearities in this case, and the results will be reported elsewhere.

4. Reconstruction of a Three-Dimensional Object

The main advantage and the real power of optical tomography come from the fact that obtaining data for 3D tomography comes basically at no extra cost as compared with 3D x-ray CT. In order to try our algorithm on experimental 3D objects, we have made

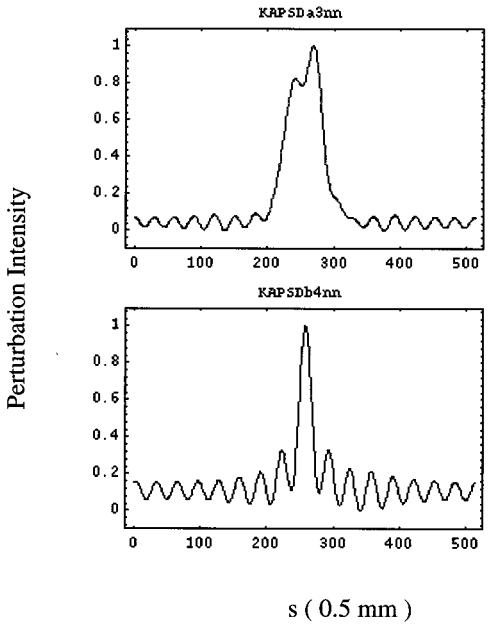

Fig. 52. Two orthogonal projections of the deblurred image given in Fig. 51. As discussed above, the oscillations around the objects are due to the crude $1/r$ filter with a sharp cutoff used in our calculations.

another set of experiments with the object shown in Fig. 53. This object was dipped in the intralipid with a metal holder, also shown in the figure. This object was then probed with the four projections described in the experimental geometry given above. Each projection was taken by 32 equally spaced source–detector pairs. In this case, we have taken a set of six measurements along the z axis as well, providing a 3D projection set. The reconstruction had to take into account the nonlinearities caused by the metal holder, which was also dipped in the intralipid. The results of the reconstructed and deblurred image is shown as an isosurface plot in Fig. 53(b).

B. Fan-Beam Tomography with Phantoms

1. Experimental Setup for Fan-Beam Projections

We performed the experiment with the fan-beam projections by placing optical fibers on the periphery of a 100-mm-diameter plastic cylinder. We used 32 source and 32 detector positions placed equally spaced from each other along the periphery of the cylinder, as shown schematically in Fig. 17. This cylinder contained drilled holes in which we could place one or two small cylindrical objects of the same material but colored for a higher absorption coefficient. We acquired the data by using a semiconductor injection laser in the NIR with 10 s of milliwatts of output power and a photomultiplier array taking 32 data points in parallel. The layout and a photo of this system are shown in Figs. 54 and 55, respectively. The data along the axis of the cylinder were acquired when the cylinder was moved up and down along its axis. Therefore the set of data taken for these experiments was 3D in the sense that the slice projections were obtained at different heights. The raw data were corrected for systematic errors that were due to the unequal detection losses in the fiber connections and the detectors.

Several examples of tomographic image reconstructions for which the fan-beam geometry was used were presented earlier[13] for planar cross sections. Below we examine a 3D reconstruction of a small cylindrical object. We have recently begun examining the images of animal tissue embedded in an intralipid. Example reconstructions through a z-plane slice of such biological phantoms are also given below.

An initial example on a 2D reconstruction that demonstrates the effects of deblurring on the appearance of the profile of a 12-mm-diameter cylindrical inhomogeneity is shown in Fig. 56. This figure demonstrates the improved resolution qualitatively, as can be deduced by the size of the contours from the brightest to the darkest areas in the images. The images were normalized to unity amplitude between the minimum and their maximums and then gray-level coded in exactly the same scale. Therefore the comparison of the size of the areas with the same gray level reveals the true size of the reconstructed object in the images. As discussed in Subsection 3.D.2, the

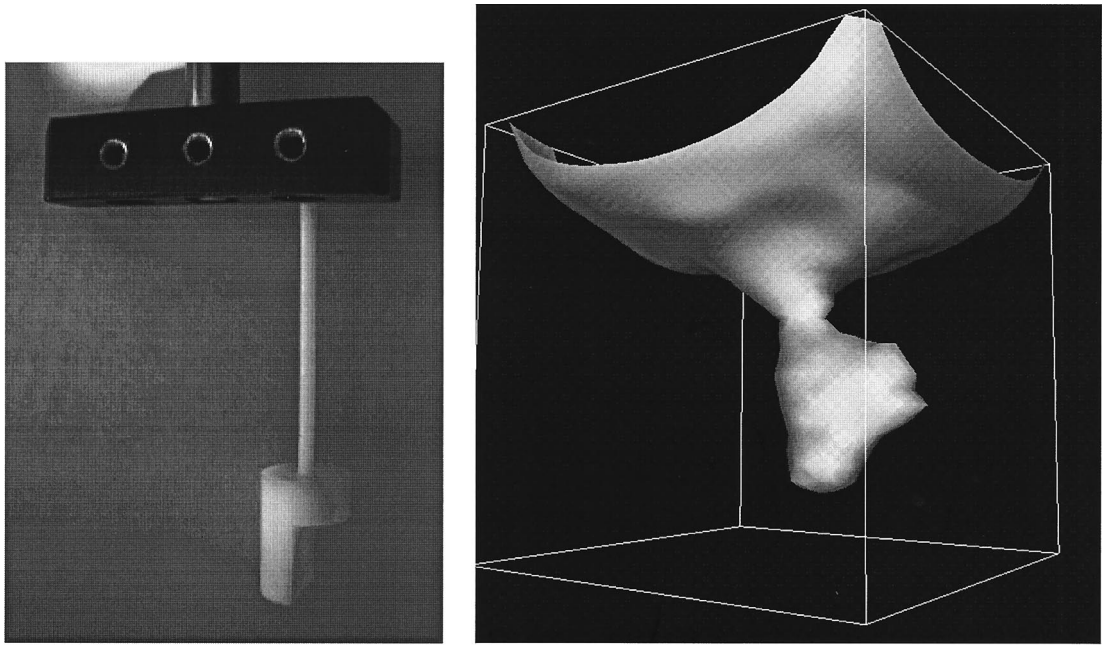

Fig. 53. (a) Picture, (b) reconstructed image of an irregular 3D object in an intralipid. As seen in (a) the object consists of an irregularly shaped Delrin material attached to a black metal holder, just above the Delrin object. The reconstructed image, shown as an isosurface plot, reproduces the shape of the object well with realistic aspect ratios. Although the effects of nonlinearities were taken into account in the image reconstruction, its distortions are still evident, with the large unrealistic boundary close to the top of the image near the metallic object.

fan-beam reconstruction images given below do not contain any corrections for $1/r$ blurring and the distortions that are due to the angular anisotropy of projections. They have no corrections for imaging nonlinearities either. As discussed also for the experimental examples for parallel-beam geometry above, the fan-beam reconstruction examples provided below are presented as a preliminary set of demonstrators for our reconstruction technique. Images constructed by taking the effects mentioned above are in preparation and they will be presented elsewhere.

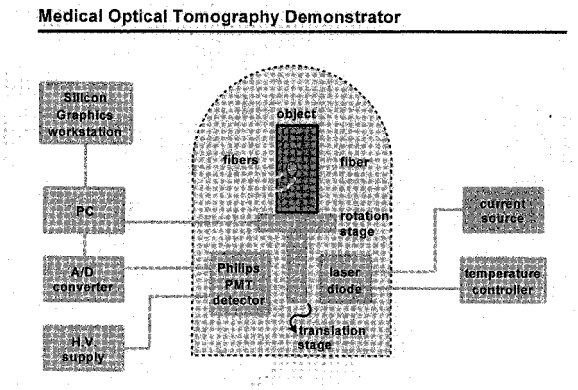

Fig. 54. Schematic system layout of the optical tomography experiments in the fan-beam geometry. A/D, analog-to-digital; H.V., high voltage; PMT, photomultiplier tube.

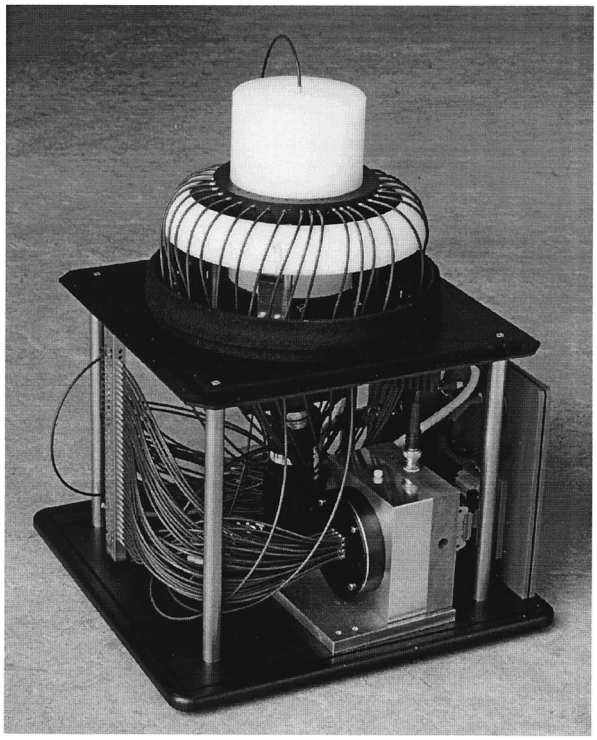

Fig. 55. Picture of the fan-beam optical tomography experimental setup. 32 equally spaced detector fibers are placed in the periphery of the ring around the cylindrical phantom. There is a single source fiber placed in the middle of two detector fiber positions. The cylindrical phantom is rotated around its axis to 32 equally spaced angles, effectively giving 32 equally spaced source positions interlaced between the detector positions.

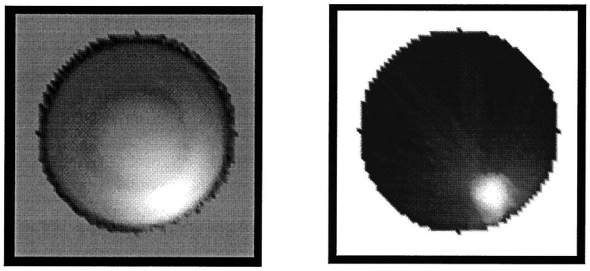

Fig. 56. Gray-level 2D tomographic image of a 12-mm-diameter cylindrical inhomogeneity probed in the fan-beam setup shown in Fig. 55. These images illustrate the effects of deblurring and provide a comparison of the original (left) and deblurred (right) images. The same gray-level coding has been applied to both images in order to provide a correct comparison to determine resolution improvements.

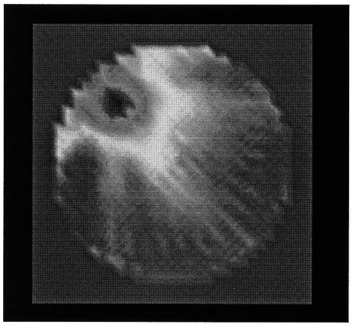

Fig. 58. Cross-sectional contour plot of the image from Fig. 57. This image provides a more realistic deblurred profile of the inhomogeneity that cannot be judged from the previous 3D isosurface plot.

2. *Experimental Results with Fan Beams: Three Dimensional*

The object studied in the 3D geometry was a small absorptive cylinder of 5-mm radius and 5-mm height placed off center in the geometry described above. The experimentally measured intensity data were converted to attenuation coefficient values and these, in return, were used for the reconstruction trials that were processed in a similar fashion as described in the paragraphs above. The details of the deblurred image reconstruction for planar fan-beam cross sections were described in Subsection 3.D.3. The cross sections for different z planes were treated separately with a final deconvolution at the end along the z direction. The reconstructed 3D image is shown in Fig. 57 as an isosurface plot. The contours of the boundary of the phantom are also shown for referencing the position of the object. The contour plot in the xy plane going through the center of the object is shown in Fig. 58. These reconstruction trials confirm the fact that the deblurring algorithm can be applied to realistic 3D images taken by practical experimental configurations. There are still some inaccuracies in the position and the width of the object, arising primarily from the noise issues discussed above.

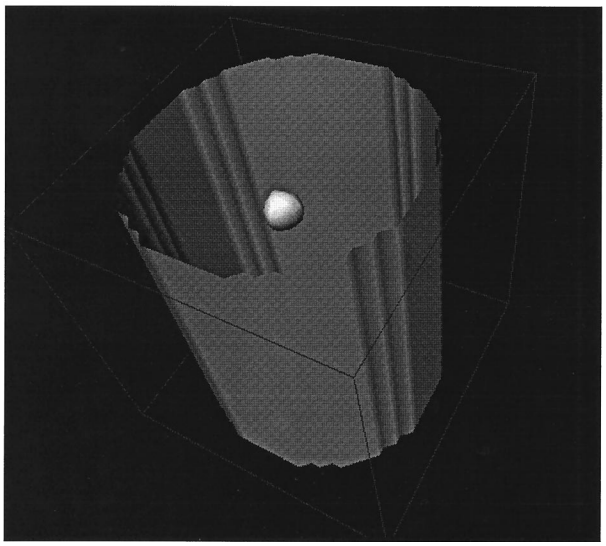

Fig. 57. 3D isosurface plot of the reconstructed image of a 5 mm $\times$ 5 mm $\times$ 5 mm absorptive cylindrical object in a nylon cylinder probed in the fan-beam geometry.

3. *Experimental Results with Animal Tissue Phantoms*

We placed chicken breast tissue in a plastic bucket and positioned it in the imaging area of the fan-beam projection setup. In the first set of experiments, there was a single piece of chicken leg with bone included between the chicken breast pieces in the phantom. The remaining empty space in the bucket was filled with intralipid with 1.2% concentration. The data were taken at a single z plane. For the measurements, we used semiconductor lasers at two different wavelengths: 787 and 670 nm. The results are given in Fig. 59. The size of the chicken leg piece is reconstructed quite realistically in the image with the dark area. The main purpose of this example is to demonstrate that any differences in the optical constants of real animal tissue, compared with

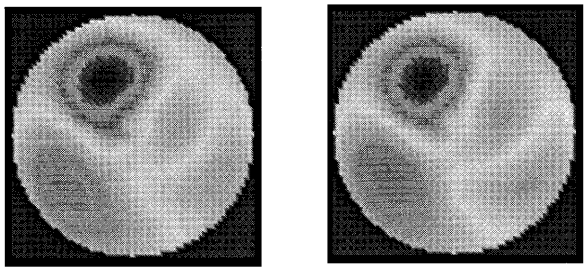

Fig. 59. Cross-sectional contour plot of a phantom containing almost fully chicken breast tissue in the fan-beam projection setup. The gaps in the bucket containing this animal tissue were filled with intralipid at 1.2% concentration. There was also a single piece of chicken leg with bone included in the phantom. The high-intensity area in the image is the location of this piece with the bone. The images are deblurred and represent measurements at two different wavelengths as indicated. The difference in the images at these two wavelengths is not strong.

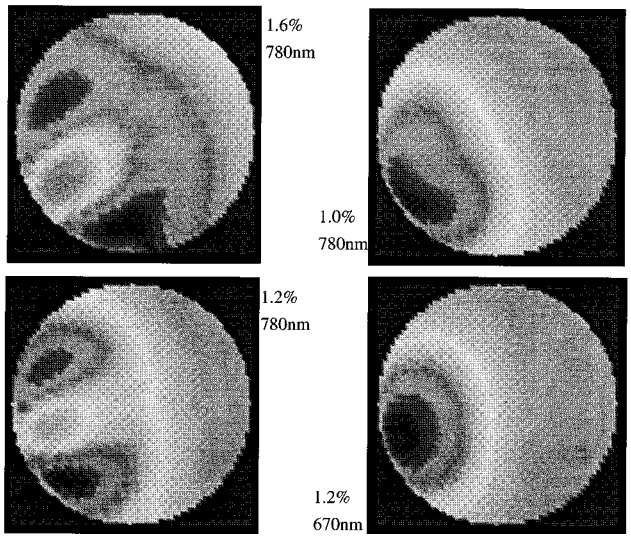

Fig. 60. Cross-sectional color-coded contour plots of a phantom containing a single piece of chicken breast meat in the fan-beam projection setup. The rest of the bucket was filled with intralipid at various concentrations. The images are not deblurred. The measurements with 1.2% intralipid were repeated at two different wavelengths, as indicated. As discussed in the text, the difference in the images reflects a differing object contrast, which changes between a scattering and an absorptive property, depending on the wavelength and the intralipid concentration. The purpose of this figure is to emphasize the differences in reconstructed images for objects that have the same physical shape but different optical parameters. With further developments in optical tomography, these differences are expected to facilitate the realization of separate images for absorption and scattering parameters, leading to a better optical diagnostics potential.

artificial phantom materials like Delrin, do not pose any problems in obtaining images.

In Fig. 59, we see that the difference in the images at the two wavelengths is not so strong. This is not, however, the case for all measurements involving different animal tissues and intralipid concentrations. This fact is demonstrated in the set of reconstructed 2D images shown in Fig. 60. There we study the differences in the images for different laser wavelengths and different intralipid concentrations with the same single piece of a nearly cylindrical chicken tissue hanging in the intralipid placed closer to the left lower corner of the image. The differences in the images are due to different types of mismatches between the optical constants of the tissue and the intralipid. These mismatches result in either more scattering or more absorbing types of perturbations from the chicken tissue within the intralipid. Because, as discussed above, the dipolar nature of the scattering perturbations can be observed in the fan-beam geometry, the differences in the images in Fig. 60 are attributed to the differences between more scattering or more absorbing contrast differences between the chicken tissue and the intralipid. These effects and other corrections coming from the boundaries in the fan-beam geometry setup are presented in Ref. 51.

5. Conclusions

In this paper we have reviewed some of the difficulties associated with image-reconstruction techniques for optical tomography in light-scattering media such as biological tissue. These difficulties are due to (1) the diffusion of photons away from their projected paths and (2) the nonlinearities in projection-image formation. The main methods available for the solution of this problem by iterative techniques are rather computation intensive. For real-time imaging applications in the clinical environment, we have developed a simple semiempirical approach, viz., a modified backprojection tomography technique. The modifications in this approach are based on the deblurring of images with deconvolution and corrections for imaging nonlinearities by coordinate transformations. As a result of our study presented in this paper we conclude that

- The resolution of optical tomographic images in diffusive media can be improved considerably when the image is deconvolved in the Fourier space during the reconstruction process. These deconvolution steps deblur the picture by compensating for the spread of the light rays between a pair of source–detector points, which is due to scattering. The shape of the blurring function is found from the statistics of photon propagation in diffuse media. The parameters necessary to compute this function are obtainable from the experimental data.
- The corrections for nonlinearities in projection-image formation can be done by empirical coordinate transformations. These corrections are necessary for cases in which high-contrast objects are present in the imaged diffusive media. Although coordinate transformations are widely used for image restoration in other fields, including medical tomography, its utilization in diffuse optical tomography has not been tried yet. In this paper we have been able to provide only a few preliminary examples of such methods applied to simple theoretical imaging cases. In these examples, by using coordinate transformation restoration, we have been able to demonstrate accurate tomographic reconstruction of images that otherwise would not be obtainable at all. However, further work is needed to explore this approach and develop it to a practical level.

As a final note, we strongly believe that a combination of such optical tomography methods, with the accumulating clinical experience on the spectroscopic signatures of normal and diseased tissue, will result in a versatile medical optical diagnosis and imaging technology in the near future. The needed knowledge for the successful realization of this optical diagnostic imaging technology lies primarily in the development of the missing spectroscopic characteristics of biomedical tissue.

References

1. D. Benaron, G. Muller, and B. Chance, "Introduction: a medical perspective at the threshold of clinical optical tomogra-

phy," in *Medical Optical Tomography: Functional Imaging and Monitoring*, G. Mueller, B. Chance, R. Alfano, S. Arridge, J. Beuthan, E. Gratton, M. Kaschke, B. Masters, S. Svanberg, and P. van der Zee, eds., Vol. IS11 of SPIE Institute Series (Society of Photo-Optical Instrumentation Engineers, Bellingham, Wash., 1993), pp. 3–9.
2. K. A. Kang, B. Chance, S. Zhao, S. Srinivasan, E. Patterson, and R. Troupin, "Breast tumor characterization using near infrared spectroscopy," in *Photon Migration and Imaging in Random Media and Tissues*, B. Chance, R. R. Alfano, and A. Katzir, eds., Proc. SPIE **1888,** 487–499 (1993).
3. R. R. Alfano, G. C. Tang, A. Pradhan, M. Bleich, D. S. J. Choy, and E. Opher, "Steady state and time resolved laser fluorescence from normal and tumor lung and breast tissues," J. Tumor Marker Oncol. **3,** 165–172 (1988).
4. D. A. Benaron, J. P. van Houten, W.-F. Cheong, E. L. Kermit, and R. A. King, "Early clinical results of time of flight optical tomography in a neonatal intensive care unit," in *Optical Tomography, Photon Migration, and Spectroscopy of Tissue and Model Media: Theory, Human Studies, and Instrumentation*, B. Chance, R. R. Alfano, and A. Katzir, eds., Proc. SPIE **2389,** 582–596 (1995).
5. F. A. Marks, H. W. Tomlinson, and J. W. Brooksby, "A comprehensive approach to breast cancer detection using light: photon localization by ultrasound modulation and tissue characterization by spectral discrimination," in *Photon Migration and Imaging in Random Media and Tissues*, B. Chance, R. R. Alfano, and A. Katzir, eds., Proc. SPIE **1888,** 500–510 (1993).
6. M. Cutler, "Transillumination as an aid in the diagnosis of breast lesions," Surg. Gynecol. Obstet. **48,** 721–730 (1929).
7. E. B. De Haller, "Time resolved breast transillumination: analytical, numerical, and experimental study," Ph.D. dissertation (Ecole Polytechnique Federal de Lausanne, Lausanne, Switzerland, 1993).
8. Y. Yamashita and M. Kaneko, "Visible and infrared diaphanoscopy for medical diagnostics," in *Medical Optical Tomography: Functional Imaging and Monitoring*, G. Mueller, B. Chance, R. Alfano, S. Arridge, J. Beuthan, E. Gratton, M. Kaschke, B. Masters, S. Svanberg, and P. van der Zee, eds., Vol. IS11 of SPIE Institute Series (Society of Photo-Optical Instrumentation Engineers, Bellingham, Wash., 1993), pp. 283–316.
9. B. B. Das, K. M. Yoo, and R. R. Alfano, "Ultrafast time-gated imaging in thick tissues: a step toward optical mammography," Opt. Lett. **18,** 1092–1094 (1993).
10. J. Kolzer, G. Mitic, J. Otto, and W. Zinth, "Measurement of the optical properties of breast tissue using time-resolved transillumination," in *Photon Transport in Highly Scattering Tissue*, S. Avrillier, B. Chance, G. J. Mueller, A. V. Preizzhev, V. V. Tuchin, and A. Katzir, eds., Proc. SPIE **2326,** 143–152 (1994).
11. M. Kashke, H. Jess, G. Gaida, J.-M. Kaltenbach, W. Wrobel, "Transillumination imaging of tissue by phase modulation," in *Advances in Optical Imaging and Photon Migration*, R. R. Alfano, ed., Vol. 21 of OSA Proceedings Series (Optical Society of America, Washington, D.C., 1994), pp. 88–92.
12. H. Jess, K. T. Moesta, G. Gaida, W. Walch, H. Erdl, P. M. Schlag, and M. Kaschke, "Optical mammography at Carl Zeiss," presented at Biomedical Optics Society Europe '95, Barcelona, Spain, 12–16 September 1995.
13. S. B. Colak, D. G. Papaioannou, G. W. 't Hooft, and M. B. van der Mark, "Optical image reconstruction with deconvolutions in light diffusing media," in *Photon Propagation in Tissues*, B. Chance, D. T. Delpy, G. J. Mueller, and A. Katzir, eds., Proc. SPIE **2626,** 306–315 (1995).
14. A. J. Devaney, "Inverse scattering theory foundations of tomography with diffracting wave fields," in *Pattern Recognition and Acoustical Imaging*, L. A. Ferrari, ed., Proc. SPIE **768,** 2–6 (1987).
15. H. Schomberg, "Nonlinear image reconstruction from projections of ultrasonic travel times and electric current densities," in *Mathematical Aspects of Computerized Tomography*, G. T. Herman and F. Natterer, eds., Vol. 8 of Springer Lecture Notes in Medical Informatics Series (Springer, Berlin, 1981), pp. 270–291.
16. T. J. Yorkey and J. G. Webster, "A comparison of impedance tomographic reconstruction algorithms," Clin. Phys. Physiol. Meas. **8,** 55–62 (1987).
17. B. Brown, D. Barber, and L. Tarassenko, eds., Special Issue on Electrical Impedance Tomography—Applied Potential Tomography, Clin. Phys. Physiol. Meas. **8,** (1987).
18. D. C. Barber and A. D. Seager, "Fast reconstruction of resistance images," Clin. Phys. Physiol. Meas. **8,** 47–54 (1987).
19. H. Schomberg, "A unifying framework for reconstructive imaging methods," in *Proceedings of the Sixth Aachener Symposium fur Signal Theorie*, D. Meyer-Ebrecht, ed., Vol. 153 of Springer Informatik-Fachberichte Series (Springer, Berlin, 1987), pp. 2–15.
20. S. R. Arridge, "The forward and inverse problems in time resolved infrared imaging," in *Medical Optical Tomography: Functional Imaging and Monitoring*, G. Mueller, B. Chance, R. Alfano, S. Arridge, J. Beuthan, E. Gratton, M. Kaschke, B. Masters, S. Svanberg, and P. van der Zee, eds., Vol. IS11 of SPIE Institute Series (Society of Photo-Optical Instrumentation Engineers, Bellingham, Wash., 1993), pp. 35–64.
21. M. Schweiger, S. R. Arridge, and D. T. Delpy, "Application of finite element method for the forward and inverse models in optical tomography," J. Math. Imag. Vision **3,** 263–283 (1993).
22. J. Chang, H. L. Graber, and R. L. Barbour, "Image reconstruction of targets in random media from continuous wave laser measurements and simulated data," in *Advances in Optical Imaging and Photon Migration*, R. R. Alfano, ed., Vol. 21 of OSA Proceedings Series (Optical Society of America, Washington, D.C., 1994), pp. 193–201.
23. M. A. O'Leary, D. A. Boas, B. Chance, and A. G. Yodh, "Experimental images of heterogeneous turbid media by frequency-domain diffusing-photon tomography," Opt. Lett. **20,** 426–428 (1995).
24. M. A. O'Leary, D. A. Boas, B. Chance, and A. G. Yodh, "Images of inhomogeneous turbid media using diffuse photon density waves," in *Advances in Optical Imaging and Photon Migration*, R. R. Alfano, ed., Vol. 21 of OSA Proceedings Series (Optical Society of America, Washington, D.C., 1994), pp. 106–115.
25. S. Rathee, Z. J. Koles, and T. R. Overton, "Image restoration in computed tomography: restoration of experimental CT images," IEEE Trans. Med. Imag. **11,** 546–553 (1992).
26. X. Wang, C. J. Ritchie, and Y. Kim, "Elevation direction deconvolution in three dimensional ultrasound imaging," IEEE Trans. Med. Imag. **15,** 389–394 (1996).
27. S. J. Glick, B. C. Penney, M. A. King, and C. L. Byrne, "Noniterative compensation for the distance dependent detector response and photon attenuation in SPECT imaging," IEEE Trans. Med. Imag. **13,** 363–374 (1994).
28. A. A. Sawchuk, "Space-variant image restoration by coordinate transformations," J. Opt. Soc. Am. **64,** 138–144 (1974).
29. A. S. McLean and J. B. Pendry, "Beyond diffusion to diffraction," J. Mod. Opt. **42,** 2495–2531 (1995).
30. G. W. 't Hooft, D. G. Papaioannou, J. J. M. Baselmans, and M. J. C. van Gemert, "Dependence of image quality on optical parameters in time-resolved transillumination experiments," in *Laser Interaction with Hard and Soft Tissue*, M. J. C. van Gemert, R. W. Steiner, L. O. Svaasand, and H. Albrecht, eds., Proc. SPIE **2077,** 153–158 (1993).
31. C. Chinnock, "Medical diagnostics: laser mammography continues development," Laser Focus World **32** (2), 38–39 (1996).
32. B. Chance, K. Kang, L. He, J. Weng, and E. Sevick, "Highly sensitive object location in tissue models with linear in-phase

and anti-phase multi-element optical arrays in one and two dimensions," Proc. Natl. Acad. Sci. USA **90,** 3423–3427 (1993).
33. D. G. Papaioannou, S. B. Colak, and G. W. 't Hooft, "Resolution and sensitivity limits of optical imaging in highly scattering media," in *Photon Propagation in Tissues*, B. Chance, D. T. Delpy, G. J. Mueller, and A. Katzir, eds., Proc. SPIE **2626,** 218–227 (1995).
34. See, for example, papers in *Medical Optical Tomography: Functional Imaging and Monitoring*, G. Mueller, B. Chance, R. Alfano, S. Arridge, J. Beuthan, E. Gratton, M. Kaschke, B. Masters, S. Svanberg, P. van der Zee, eds., Vol. IS11 of SPIE Institute Series (Society of Photo-Optical Instrumentation Engineers, Bellingham, Wash., 1993).
35. D. Boas, M. O'Leary, and A. Yodh, University of Pennsylvania, Photon Migration Imaging (PMI) Software Package; User's information is available on the Internet. The source code is available by anonymous ftp at sol1.lrsm.upenn.edu in /pub/pmi.
36. S. L. Jacques, M. R. Ostermeyer, L. Wang, and A. H. Hielscher, "Effects of sources, boundaries, and heterogeneities on photon migration," in *Advances in Optical Imaging and Photon Migration*, R. R. Alfano, ed., Vol. 21 of OSA Proceedings Series (Optical Society of America, Washington, D.C., 1994), pp. 83–87.
37. M. R. Ostermeyer, S. L. Jacques, A. H. Hielscher, and L. Wang, "Accelerated modeling of light transport in heterogeneous tissue using superposition of virtual sources," in *Photon Transport in Highly Scattering Tissue*, S. Avrillier, B. Chance, G. J. Mueller, A. V. Priezzhev, V. V. Tuchin, and A. Katzir, eds., Proc. SPIE **2326,** 56–64 (1995).
38. M. R. Ostermeyer and S. L. Jacques, "Perturbation theory for optical diffusion theory: a general approach for absorbing and scattering objects in tissue," in *Optical Tomography, Photon Migration, and Spectroscopy of Tissue and Model Media: Theory, Human Studies, and Instrumentation*, B. Chance, R. R. Alfano, and A. Katzir, eds., Proc. SPIE **2389,** 98–102 (1995).
39. J.-M. Kaltenbach and M. Kaschke, "Frequency- and time-domain modelling of light transport in random media," in Ref. 34, pp. 65–86.
40. S. Feng, F. Zeng, and B. Chance, "Monte Carlo simulations of photon migration path distributions in multiple scattering media," in *Photon Migration and Imaging in Random Media and Tissues*, B. Chance, R. R. Alfano, and A. Katzir, eds., Proc. SPIE **1888,** 78–89 (1993).
41. E. M. Sevick, C. L. Burch, J. K. Frisoli, M. L. Johnson, K. Nowaczyk, H. Szmacinski, and J. R. Lakowicz, "The physical basis of biomedical optical imaging using time-dependent measurements of photon migration in the frequency domain," in Ref. 34, pp. 485–512.
42. D. H. Burns, "Optical tomography for three-dimensional spectroscopy," Appl. Spectrosc. **48,** 12A–19A (1994).
43. L. T. Perelman, J. Wu, I. Itzkan, Y. Wang, R. Dasari, and M. S. Feld, "Photon paths in turbid media: theory and experimental observation," in *Advances in Optical Imaging and Photon Migration*, R. R. Alfano, ed., Vol. 21 of OSA Proceedings Series (Optical Society of America, Washington, D.C., 1994), pp. 153–155.
44. A. Hielscher and F. K. Tittel, "Photon density wave diffraction tomography," in *Advances in Optical Imaging and Photon Migration*, R. R. Alfano, ed., Vol. 21 of OSA Proceedings Series (Optical Society of America, Washington, D.C., 1994), pp. 78–82.
45. F. Natterer, *The Mathematics of Computerized Tomography* (Wiley, New York, 1986), Chap. V, pp. 128–137.
46. D. C. Youla, "Mathematical theory of image restoration by the method of convex projections," in *Image Recovery: Theory and Application*, H. Stark, ed. (Academic, New York, 1987), Chap. 2.
47. See R. R. Alfano, ed., *Advances in Optical Imaging and Photon Migration*, Vol. 21 of OSA Proceedings Series (Optical Society of America, Washington, D.C., 1994).
48. See papers in *Tissue Optics—Applications in Medical Diagnostics and Therapy*, V. V. Tuchin, ed., Vol. MS102 of SPIE Milestone Series (Society of Photo-Optical Instrumentation Engineers, Bellingham, Wash., 1994).
49. S. W. Rowland, "Computer implementation of image reconstruction formulas," in *Image Reconstruction from Projections*, G. T. Herman, ed. (Springer-Verlag, Berlin, 1979), pp. 9–79.
50. S. A. Walker, A. E. Cerussi, and E. Gratton, "Back-projection image reconstruction using photon density waves in tissues," in *Optical Tomography, Photon Migration, and Spectroscopy of Tissue and Model Media: Theory, Human Studies, and Instrumentation*, B. Chance, R. R. Alfano, and A. Katzir, eds., Proc. SPIE **2389,** 350–357 (1995).
51. M. B. van der Mark, G. W. 't Hooft, D. G. Papaioannou, S. B. Colak, N. A. A. J. van Asten, and J. C. J. Paasschens, "Boundary effects in optical tomography," presented at Biomedical Optics Society Europe '96, Vienna, 7–11 September 1996.